Study of the Effect of Uncertainties of HEAT Calibration on Data Analysis

von

Oskar Hofmann

Bachelorarbeit in Physik

vorgelegt der
Fakultät für Mathematik, Informatik und Naturwissenschaften
der
Rheinisch-Westfälischen Technischen Hochschule Aachen

im August 2012

angefertigt am

III. Physikalischen Institut A

Gutachter und Betreuer

Prof. Dr. Thomas Hebbeker
III. Physikalisches Institut A
RWTH Aachen

Contents

List of Figures

1. Introduction

In 1912 Victor Hess measured ionizing radiation up to an altitude of 5300 m. He discovered an increase in radiation above 1000 m which led him to the interpretation of a very penetrative radiation from above the atmosphere [1]. Robert Andrew Millikan coined the term "cosmic rays" during his own experiments in the 1920s to describe this extraterrestrial radiation. While Millikan believed in high energy photons to be the primary particles of the cosmic rays, several experiments in the 1930s and 1940s showed that cosmic rays consist of charged particles, mostly protons and other nuclei [2].

If cosmic ray primary particles interact with the earth's atmosphere, they are able to produce a cascade of secondary particles called "extensive air showers". This was shown by Pierre Auger et al. who measured coincidences between Geiger-Müller counters depending on the distance between the counters in 1939. They were able to detect coincidences with distances up to 300 m, which indicate primary particles with an energy of up to 10^{15} eV [3].

In contrast to detectors which directly detect particles from extensive air showers, fluorescence detectors use a different approach to measure cosmic rays. Charged secondary particles from an extensive air shower are able to excite the atmospheric nitrogen along their path. By detecting the light from the deexcitation of the nitrogen, fluorescence detectors are able to observe the longitudinal development of air showers. On the one hand this technique improves the resolution of the shower energy. On the other hand it offers only a relatively small duty cycle as it is dependent on a dark environment, e.g. moonless and starlit nights. The first full-scale fluorescence experiment was performed in 1967 by Kenneth Greisen et al. [4].

The *Pierre Auger Observatory* combines the ideas of an array of particle detectors and fluorescence detectors to a hybrid detector. It covers an area of 3000 km^2 in the Argentine Pampa. Hence, it is the largest detector of its kind and designed to measure extensive air showers in the energy range from 10^{18} to 10^{20} eV and above. Even before the completion of the Observatory in 2008 one began to build extensions to expand the observable shower energy range down to 10^{17} eV. One of these extensions are the *High Elevation Auger Telescopes* (HEAT).

While HEAT is taking data since May 2010 the absolute energy calibration for the telescopes is still work in progress. A preliminary calibration was performed and allows to analyse the already taken data. This work is based on this preliminary calibration and studies the effect of varying the HEAT calibration constants within their uncertainties on the event reconstruction and data analysis. This is done by presenting an analysis of the change of shower parameters due to the altering of the calibration constants.

The chapters 2 and 3 give an introduction into Cosmic Rays and the Pierre Auger Observatory. Next, chapter 4 describes in detail the approach of this work. The impact of altered calibration constants on the reconstructed shower geometry is shown in chapter 5 while chapter 6 analyses the impact on the reconstructed shower energy and shower maximum.

2. Cosmic Rays

2.1 Energy Spectrum

The flux of cosmic ray particles depends on the energy of the particles. Fig. 2.1 shows the all-particle energy spectrum from 10^{10} eV to the highest measurable energies. The flux can be approximated by a broken power law $\mathrm{d}N/\mathrm{d}E \propto E^{\gamma}$ with the spectral index γ. While the spectrum is described with a spectral index $\gamma = -2.7$ until the *knee* at $\approx 4.5 \cdot 10^{15}$ eV, it steepens there to $\gamma = -3.1$. One common explanation for this kink in the spectrum is that $E_k \approx 4.5\,\mathrm{PeV}$ is the highest energy, protons can achieve naturally within our galaxy. Elements with a higher charge number Z can therefore reach energies up to $E = Z \cdot E_k$ [5]. The knee corresponds to a particle flux of 1 particle per m^2 per year. The spectral index changes again at the *second knee* at $4 \cdot 10^{17}$ eV to $\gamma \approx -3.3$ and flattens again at the *ankle* at $4 \cdot 10^{18}$ eV to $\gamma \approx -2.7$ [6]. At this point the flux decreases to 1 particle per km^2 and year.

Due to the low flux of cosmic rays at high energies, direct measurements of particles are limited by detector size to energies below 10^{15} eV. For higher energies one measures the secondary particles produced in the earth's atmosphere at ground level or uses the the atmosphere as calorimeter with the help of fluorescence telescopes.

2.2 Sources of Cosmic Rays

The sources of ultra high energetic cosmic rays are still subject of actual research. One common theory for the acceleration of particles to high energies is the shock acceleration in supernovae explosions [7]. This theory describes how particles are accelerated multiple times while crossing certain electro-magnetic domains in the shock-front of supernovae. Another type of models that describe the origin of ultra high energy particle are the Top-Down-Models, which assume currently unknown very heavy particles which decay into known particles with high energies [8].

2.3 Extensive Air Showers

A high energy cosmic ray particle which enters the earth's atmosphere interacts with molecules in the atmosphere producing several secondary particles. These secondary particles interact with the atmosphere as well, which leads to a cascade of new reactions and particles. This is called an *extensive air shower* (EAS).

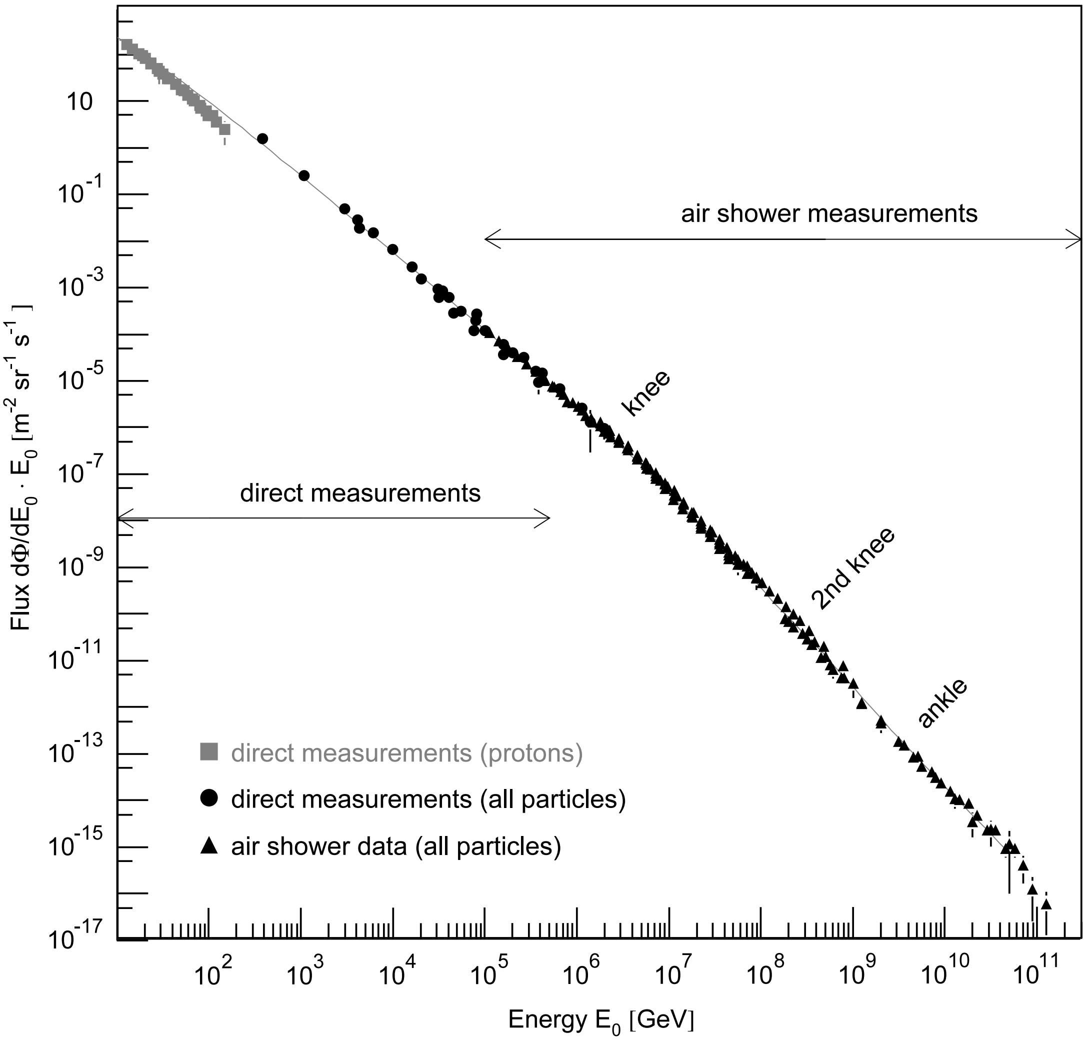

Figure 2.1: All-particle energy spectrum of cosmic rays as measured directly with detectors above the atmosphere and with air showers detectors. [5]

2.3.1 Atmospheric Depth

As the interaction of particles depends on the cross-sections of the involved processes and therefore on the amount of traversed matter, it is reasonable to introduce the concept of atmospheric depth $X(s)$. It is defined as the path integral

$$X(s) = \int_s \rho(x)\,\mathrm{d}x \tag{2.1}$$

along the path of the particle with the atmospheric density ρ at point x. $X(s)$ has the unit $\mathrm{g\,cm^{-2}}$ with $0\,\mathrm{g\,cm^{-2}}$ at the top of the atmosphere and $\approx 1000\,\mathrm{g\,cm^{-2}}$ at sea level (for a vertical path).

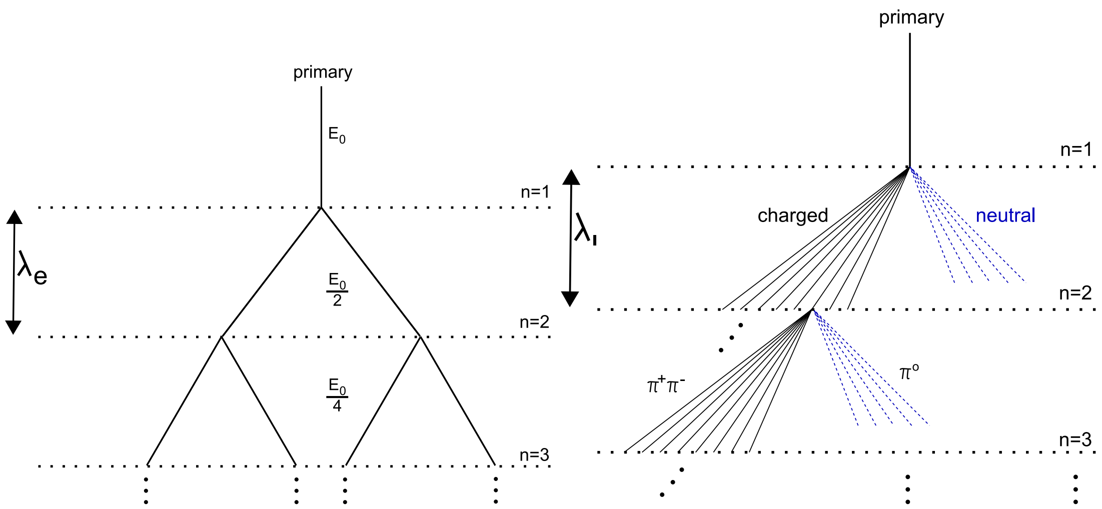

(a) Electromagnetic Heitler model [9] **(b)** Hadronic Heitler-Matthews model [9]

Figure 2.2: Development of electromagnetic (a) and hadronic extensive air showers (b)

2.3.2 Heitler-Model

A very illustrative model to describe the development of an EAS is the electromagnetic Heitler-Model [9],[10]. It assumes that an e.m. particle ($e^{\pm}$, photon) with energy E travels a depth distance λ_e before producing two new particles with energy $E/2$ (cf. fig. 2.2a). Hence the number of particles doubles every λ_e until the single particle energy falls below the critical energy $E_c \approx 85\,\mathrm{MeV}$. Below E_c, energy loss due to ionization dominates over particle production. Therefore, the maximum number of particles in the shower is

$$N_{\mathrm{max}} = E_0/E_{\mathrm{c}} \;\propto\; E_0 \tag{2.2}$$

with the energy of the primary particle E_0. As the number of particles as a function of atmospheric depth is given by $N(X) = 2^{X/\lambda_{\mathrm{em}}}$, the atmospheric depth of the shower maximum X_{max} can be calculated as

$$X_{\mathrm{max}}^{\mathrm{em}} = \lambda_{\mathrm{e}} \cdot \log_2(E_0/E_{\mathrm{c}}) \;\propto\; \log(E_0) \tag{2.3}$$

2.3.3 Hadronic Extension of the Heitler Model

The Heitler model can be extended to describe hadron-initiated showers, e.g. to the Heitler-Matthews-Model [11]. It assumes, that a proton with energy E_0 produces n_{tot} new particles with energy E_0/n_{tot}. About one third of these particles are neutral π^0 which decay immediately into two photons inducing electromagnetic showers. The remaining particles are charged $\pi^{\pm}$. If their energy is above a critical energy E_{dec} they travel the interaction length λ_{I} before reinteracting with the atmosphere and starting a new particle generation (cf. fig. 2.2b), otherwise they decay into muon-neutrino pairs before travelling λ_{I} .

The observable fluorescence light is mainly emitted by the electromagnetic shower component. Hence the X_{max} of a hadron-induced shower is given by that of the electromagnetic sub-showers. If the primary is a nucleus with mass number A the shower can be approximated by the superposition of A proton induced showers with energy E_0/A. This leads to the depth of shower maximum

$$X_{\mathrm{max}}^{A} \approx X_{\mathrm{max}}(E_0/A) \;\propto\; \log(E_0/n_{\mathrm{tot}}) - \log(A) \tag{2.4}$$

Therefore X_{max}, together with the energy of the shower, is indicative of the mass of the primary particle and allows to study the mass composition of the cosmic rays.

3. The Pierre Auger Observatory

The Pierre Auger Observatory [12] is a cosmic ray observatory in the Pampa Amarilla in Argentina next to the town of Malargüe. With an observed area of 3000 km^2 it is the largest observatory of its kind and able to detect ultra-high-energy cosmic rays with a flux of less then 1 particle per km^2 and century. The observatory was designed to measure cosmic ray particles with energies from 10^{18} to 10^{20} eV and above and to determine their spectrum, mass composition and arrival directions. For this purpose it combines two complementary detector types: a surface detector and a fluorescence light detector.

3.1 Surface Detector

The surface detector (SD) consists of 1600 autonomous water Cherenkov detector stations with a spacing of 1500 m (cf. fig. 3.1). Each station contains 12 m^3 of pure water and three photomultiplier tubes (PMTs) detecting Cherenkov light produced by traversing particles. The stations are powered by batteries charged via two solar panels and provide an uptime of nearly 100 %.

Data taken at each detector is preliminary checked for possible shower candidates and, where trigger conditions are fulfilled, sent wirelessly to a central data acquisition system (CDAS) for further analyses. The single stations, their communication system and the trigger algorithm are documented in [13] and [14].

3.2 Fluorescence Detector

The fluorescence detector (FD) of the Pierre Auger Observatory oversees the area of the SD with 24 telescopes. Each telescope has a field of view (FoV) of 30° x 30° in azimuth and elevation. Six telescopes are combined to a so called "eye" giving each eye a coverage of 180° in azimuth and 30° in elevation (cf. fig. 3.1). The FD is designed to detect the fluorescence light from EAS evolving above the SD with a trigger efficiency of 100 % for showers with energies above 10^{19} eV within a distance of around 30 km. It is described in more detail in [15].

The observed fluorescence light is produced by charged secondary particles (mostly $e^{\pm}$) from the EAS. They deposit their energy by excitation or ionization of nitrogen or other molecules in the atmosphere. While relaxing to the ground state, these molecules isotropically emit fluorescence light in the UV range (300 to 430 nm). This allows to observe the shower from all sides. Other kinds of light from the

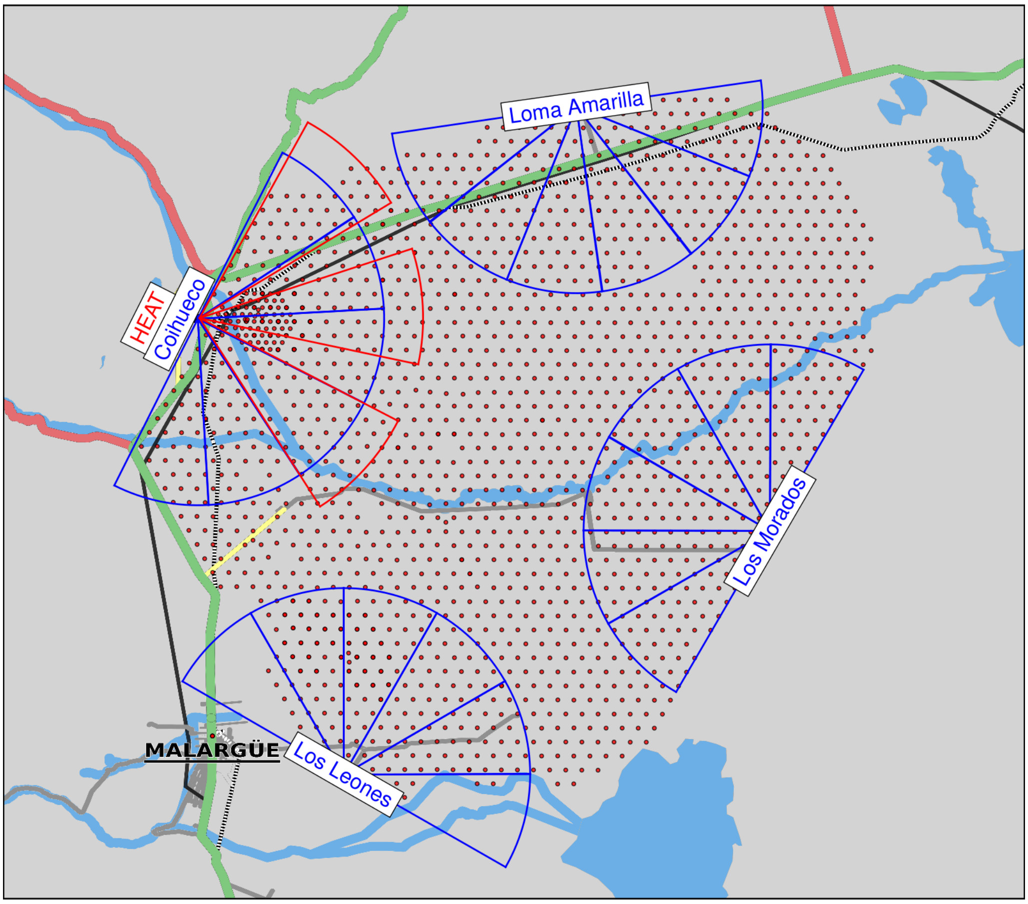

Figure 3.1: Map of the Pierre Auger Observatory in Argentina. The red dots mark the positions of the SD stations. The four conventional FD eyes including their azimuthal field of view are plotted in blue. Next to Coihueco, the field of view of the three HEAT telescopes is marked in red. Drawing by courtesy of Marcel Straub (RWTH Aachen).

shower, like Cherenkov light, is observed by the telescopes as well and has to be considered during the energy reconstruction.

3.2.1 Hardware

The individual telescopes are located in a clean and air-conditioned room (cf. fig. 3.2). The light enters the room through an UV-filter which prevents the telescope from being saturated by visible light. The telescope itself is a Schmidt camera: A segmented mirror reflects the incoming light onto the camera which consists of 440 pixels. As Schmidt cameras have a curved focal plane the pixels are also arranged curved, each providing a FoV of 1.5° [15]. A shutter in front of the UV-filter can be closed to prevent the telescope from being exposed to a too high light flux e.g. during daylight.

The pixels of the camera are organized in 22 rows and 20 columns and in ten groups of 44 pixels. Each pixel consists of a hexagonal PMT with a light collector to reduce the dead space between the pixels. The PMTs of each group have very similar

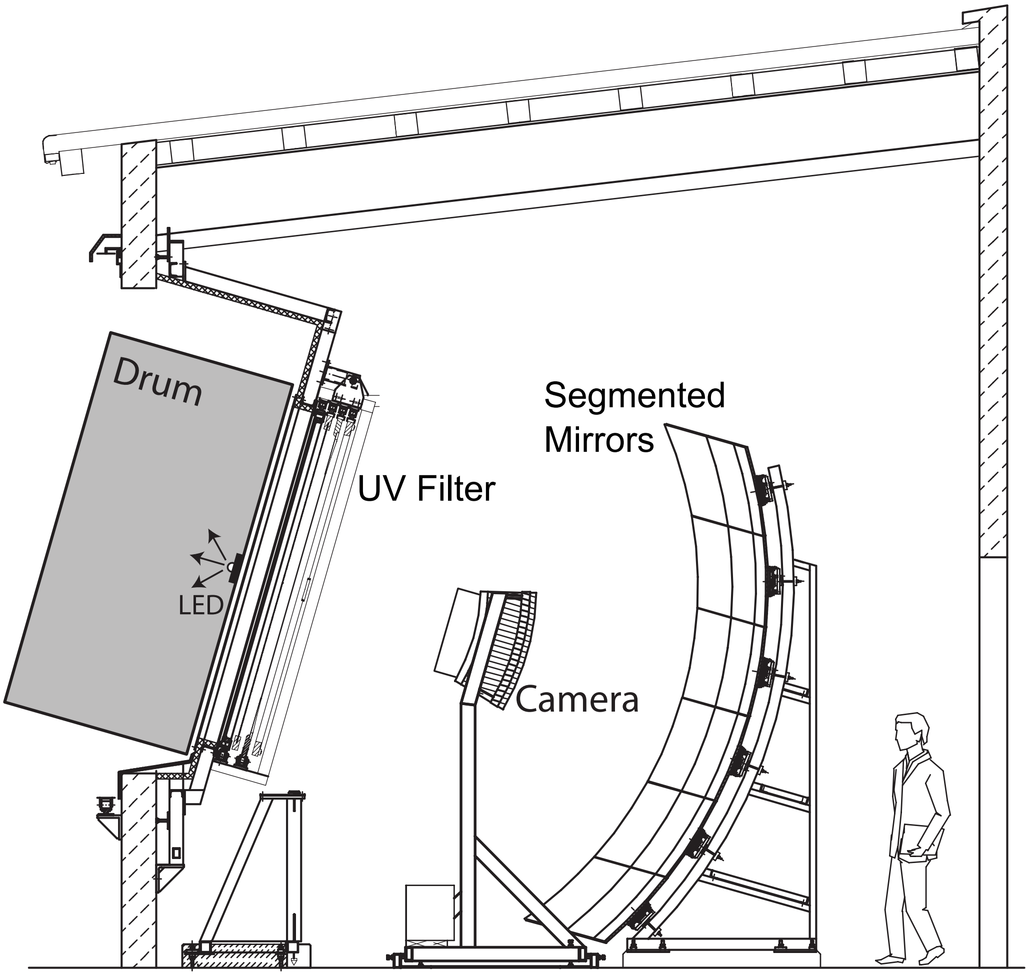

Figure 3.2: Schematics of one Auger fluorescence telescope with calibration drum at aperture. The drum is only attached for calibration measurements. Adapted from [15].

characteristics (due to selection after characterization) and therefore are powered by one single high voltage channel.

The signal of each pixel is continuously read out by an FADC (flash analog-to-digital converter) and digitized with a sampling rate of 10 MHz. This corresponds to a 100 ns FADC bin size. The digitized signal is then processed by a trigger system. Triggered events are read out by the MirrorPC, the control computer of each telescope. The data of all telescopes is fed into the EyePC which finally merges all data into one event. The EyePC also communicates with the CDAS (cf. sec. 3.1).

3.2.2 Telescope Calibration

The reconstruction of the longitudinal profile of an EAS and the ability to determine the energy deposit in the atmosphere depend on being able to convert the ADC counts into a light flux at the aperture of the telescope. Therefore an absolute calibration of each telescope is needed. The calibration of the fluorescence detectors at the Pierre Auger Observatory uses a calibrated light source with a diameter of

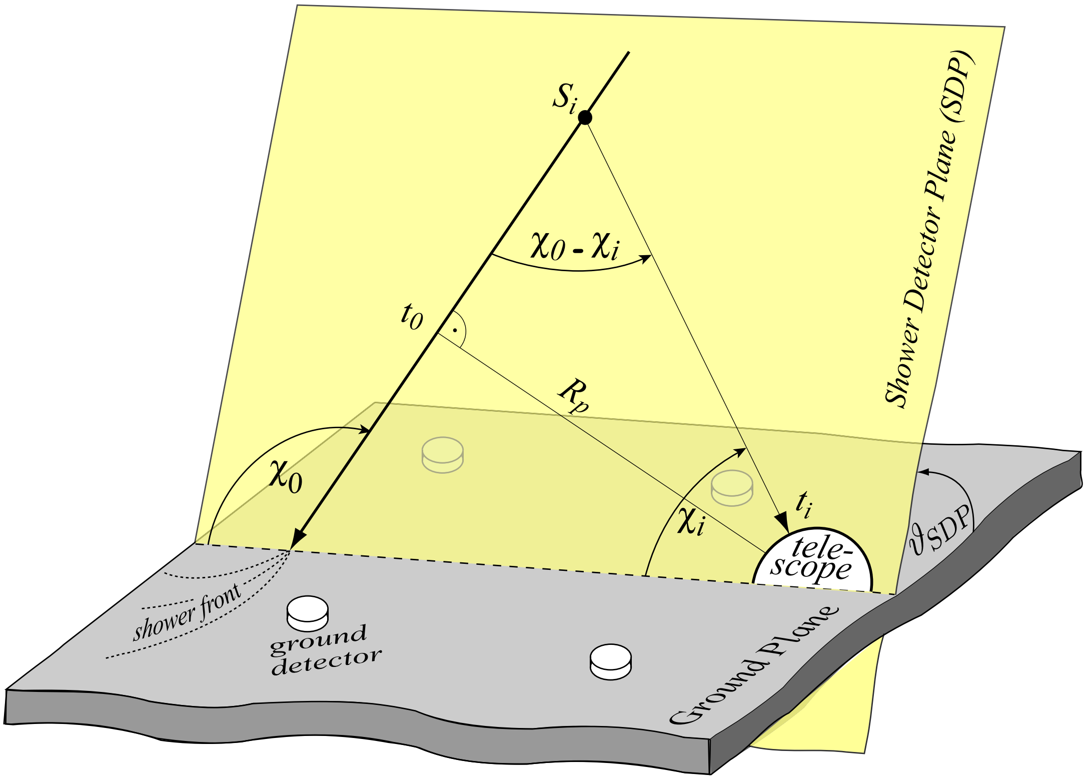

Figure 3.3: Illustration of the geometrical shower reconstruction from the observables of the fluorescence detector. Adapted from [16]

2.5 m at the aperture of the telescope (cf. fig. 3.2). This so called "drum" provides the same known flux of light at each pixel of the camera [15].

Flat Fielding

The first step of the calibration is the flat fielding of the telescope. As the drum delivers an uniform light flux an uniform output signal from the PMTs is expected. Therefore the gain of the PMTs is adjusted to get an as uniform output as possible. This adjustment is only possible in groups of 44 PMTs because all PMTs in one group have the same power supply (cf. sec. 3.2.1).

Absolute Calibration

With the known light flux from the drum it is then possible to calculate the number of photons that correspond to each ADC count. This is done for each individual PMT and then implemented in the event reconstruction. The average response of the FD is approximately 5 photons/ADC bin.

3.3 Event Reconstruction

The reconstruction of events using data from SD and FD is called hybrid reconstruction. The analysis framework of the Pierre Auger Observatory used for hybrid reconstruction is the Auger $\overline{\text{Off}}\underline{\text{line}}$ software package [17]. $\overline{\text{Off}}\underline{\text{line}}$ is an analysis framework written in C++ and is used for event reconstruction as well as for detector simulation. All steps in the reconstruction of events or the simulation of the detector are performed by single modules. The order and configuration of the modules can be controlled by so called steering cards. This makes $\overline{\text{Off}}\underline{\text{line}}$ highly flexible.

The hybrid reconstruction of an EAS is based on the light measured by the FD and the position and timing of the SD station with the highest signal. The FD ADC traces are baseline corrected by subtracting the mean of each trace and then converted into photon traces using the respective calibration constants. The first step in the geometry reconstruction is the determination of the shower-detector plane (SDP). The SDP is the plane containing the FD, that detected the shower, and the shower axis (cf. fig. 3.3). Using the timing information of the FD pixel and the SD station, the shower axis $\hat{S}$ is determined within the SDP using a χ^2 minimization [16]. As a result of this minimization the parameters χ_0, R_p and t_0 of the shower axis are received. χ_0 is the angle relative to the horizontal plane within the SDP. R_p is the closest distance between shower axis and detector whereas t_0 is the timing at which the shower passes this point of closest distance.

For the reconstruction of the shower energy the contribution of fluorescence light is calculated from the measured light flux. The energy deposit per atmospheric depth dE / dX is determined fitting a four parameter Gaisser-Hillas function [18] on the light profile

$$\frac{\mathrm{d}E}{\mathrm{d}X}(X) = \left.\frac{\mathrm{d}E}{\mathrm{d}X}\right|_{X=X_{\max}} \left(\frac{X - X_0}{X_{\max} - X_0}\right)^{\frac{X_{\max}-X_0}{\lambda}} e^{\frac{X_{\max}-X}{\lambda}} \tag{3.1}$$

with the depth of maximum energy deposit $X_{\max}$ and the maximum energy deposit per atmospheric depth $\mathrm{d}E/\mathrm{d}X|_{X=X_{\max}}$. X_0 and λ are additional interaction parameters.

The integral over this longitudinal shower profile is the total calorimetric energy E_{cal} which is about 90 % of the energy E_0 of the primary. The remaining 10 % are carried by neutrinos and muons produced in the shower and are not visible for the FD [19].

3.4 High Elevation Auger Telescopes (HEAT)

As the standard FD and SD of the Pierre Auger Observatory are designed to measure EAS with energies of 10^{18} eV and above, several extensions were build to expand the energy range down to 10^{17} eV (cf. [21]). One of these extensions are the *High Elevation Auger Telescopes* (HEAT). HEAT allows to observe an energy range, where the transition from primaries of galactic origin to those of extragalactic origin is expected [6]. By observing the depth of the shower maximum $X_{\max}$, it is possible to conclude the mass composition of the primaries in this energy region (cf. sec. 2.3.3).

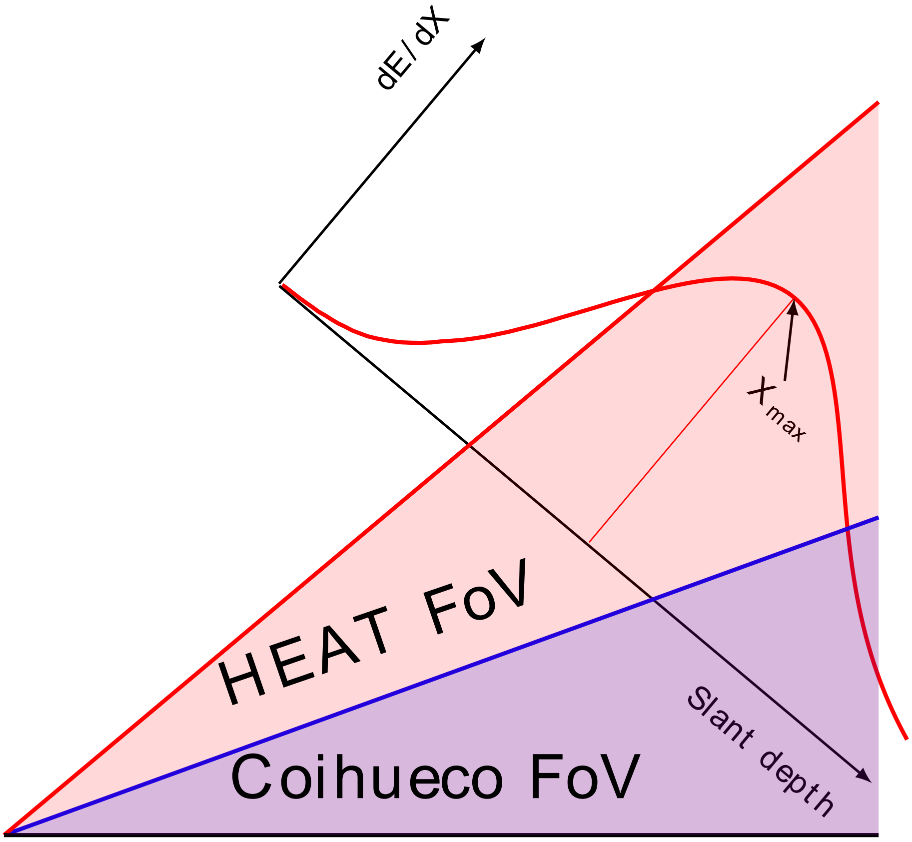

Figure 3.4: Combined field of view (FoV) of a regular Auger FD telescope (Coihueco) and HEAT. The shown angles are not to scale. Additionally, the longitudinal energy deposit profile of a shower, which is only fully reconstructible in the HEAT extended FoV, is shown. [20]

Showers with lower energy reach their maximum higher in the atmosphere because the critical energy per secondary is reached earlier (cf. eq. (2.3)). As the reconstruction of an EAS with FD heavily relies on the observation of the depth of the shower maximum X_{max}, it was necessary to expand the FoV of the standard FD to lower atmospheric depths. HEAT consists of three standard Auger FD telescopes mounted in tiltable housings. These housings can be tilted by 30° upwards allowing HEAT to observe EAS induced by lower energy primaries (cf. fig. 3.4). HEAT is close to the standard FD eye *Coihueco* (cf. fig. 3.1). If HEAT operates in the tilted (upward) mode the FoV of HEAT and Coihueco are complementary. Therefore, the fluorescence light traces of showers observed by HEAT and/or Coihueco are combined into a virtual eye called *CoHe* for a combined reconstruction.

3.4.1 Hardware

Due to the fact that HEAT looks higher in the atmosphere, more showers close to the telescope are observed [20]. As closer showers have a higher angular velocity a higher sampling rate is needed to ensure a good temporal and geometrical resolution. Whereas the signal of a PMT of standard FD is digitized with a sampling rate of 10 MHz, the electronics used for HEAT supports a sampling rate of up to 40 MHz.

At the present time, the HEAT FADCs are operated with a sampling rate of 20 MHz corresponding to a 50 ns FADC bin size.

3.4.2 Calibration

The HEAT telescopes are calibrated like the standard FD telescopes (cf. sec. 3.2.2). While the flat fielding was already performed the absolute calibration for the three telescopes is still work in progress. The calibration measurements using the drum are taken but not yet evaluated.

To be able to analyse HEAT data, before the final calibration is implemented into the $\overline{\text{Off}}\underline{\text{line}}$ framework, a preliminary cross-calibration with Coihueco was performed by S. Falk, D. Kruppke-Hansen et al. from the *Karlsuher Institut für Technologie* and the *Bergische Universität Wuppertal.* Therefore, the small fraction of events where HEAT was not tilted (downward mode) and recorded showers was evaluated and compared to the reconstructions of the same events recorded by Coihueco [22]. This led to a single calibration constant for each telescope. Since HEAT was already flat-fielded this calibration is used for all pixels of each telescope. The results of this cross-calibrations are:

$$\begin{aligned} c_{\mathrm{tel1}} &= (2.65 \pm 0.03)\ \mathrm{photons/ADC} \\ c_{\mathrm{tel2}} &= (2.36 \pm 0.04)\ \mathrm{photons/ADC} \\ c_{\mathrm{tel3}} &= (2.52 \pm 0.03)\ \mathrm{photons/ADC} \end{aligned} \tag{3.2}$$

Due to the doubled sampling rate compared to standard FD an average response of about 2.5 photons/ADC bin is expected.

4. Study of the Effect of HEAT Uncertainties

While HEAT is taking data since May 2010 the analysis of this data is only possible with a preliminary energy calibration of the telescopes, determined from a cross-calibration with the nearby eye Coihueco (cf. sec. 3.4.2). Besides, this cross-calibration was performed with low statistics (less than 120 events per HEAT telescope). This work studies the effect of the uncertainties of the HEAT calibration constants (cf. eqn. (3.2)) on the event reconstruction and data analysis.

The analysis is performed on a data sample taken from 01/12/2010 until 28/02/2011, after the last flat fielding of HEAT in November 2010 (cf. sec. 3.2.2), using events measured by HEAT and/or Coihueco. To determine the systematic uncertainties on reconstructed shower parameters (like geometry and energy) arising from the uncertainties of the HEAT calibration, multiple reconstructions of each event are done. These events are reconstructed with the $\overline{\text{Off}}\underline{\text{line}}$ analysis framework in version v2r2p7 with the standard calibration as well as with changed HEAT calibration constants. The calibration of the standard FD telescopes is not changed at all. For each reconstruction with an altered HEAT calibration, the values of selected reconstructed quantities are compared to those of a reconstruction with the standard calibration. This allows to analyse the impact of changing the HEAT calibration constants within their statistical uncertainties on the reconstruction of an EAS. For the change of the HEAT constants it was decided to uniformly increase or decrease the calibration constants of each HEAT telescope by 1, 3, 5 and 10 standard deviations of the respective calibration constant. One standard deviation σ corresponds to a change of the calibration constants of about 1.3 %. A deviation of up to five σ is conceivable for Gaussian uncertainties whereas a change of 10 σ is done to check for an expected linear correlation of calibration constants and e.g. reconstructed energy and for unexpected major changes in the reconstruction of the showers.

Additionally, the impact of HEAT uncertainties on the event reconstruction is analysed separately for HEAT-only and combined HEAT and Coihueco events. Therefore, it is possible to identify effects caused not only by the change of the HEAT calibration but also by the combined reconstruction of HEAT and Coihueco data. Standard analysis cuts are applied on all events (cf. tab. 4.1).

In the next two chapters the impact of the uncertainty on the HEAT calibration constants on reconstructed shower properties is shown and analysed. The analysis of the shower parameters is divided into two parts: the analysis of the low-level parameters and the analysis of the high-level parameters. The low-level parameters mainly include the geometry of the showers, which are the first parameters reconstructed using mainly the timing information of FD and SD. The high-level parameters are gained by fitting the Gaisser-Hillas function (eqn. (3.1)) on the energy deposit profile of the event using the energy calibration of the telescopes. This work focuses on the shower energy E and the depth of the shower maximum X_{max} as high-level parameters.

4.1 Offline Module Sequence

As described in sec. 3.3, the Offline framework consists of several modules. The following section gives an overview of the modules used for the FD hybrid reconstruction (adapted from [20]). The modules are listed in the same order as they are called up in the reconstruction sequence.

FdCalibrator corrects each camera pixel for noise and applies the calibration constant to convert the FD ADC traces to photon traces. This module uses the *FFixCalibConfig* allowing to adapt the calibration constants for standard FD and HEAT. For this work the *FFixCalibConfig* is used to alter the HEAT calibration constants as stated above. The calibration of standard FD stays untouched.

FdEyeMergerKG merges data from Coihueco and HEAT telescopes for a combined analysis in the virtual *CoHe* eye.

FdPulseFinder determines the pulse centroid in time from the ADC trace of each pixel.

FdSDPFinder determines the shower detection plane (SDP) from the triggered pixels.

FdAxisFinder transforms the pointing of pixel i to angle χ_i (cf. fig. 3.3) and calculates the shower axis in the SDP.

HybridGeometryFinderOG uses the previously reconstructed shower geometry parameters of each telescope as initial values for a fit of χ_0, R_p and t_0 over all available telescopes in each eye. The timing information of the triggered SD station with the highest signal in a maximum distance of 2000 m to the shower core is used as well.

HybridGeometryFinderWG uses geometry parameters from previous modules as initial values to perform a fit on all telescopes present in the virtual eye.

FdApertureLightFinderKG calculates, based on the geometrical reconstruction, the longitudinal light profile for each telescope.

FdEnergyDepositFinderKG determines the Cherenkov and fluorescence ratio of the light trace. Based on the fluorescence light, the energy deposit profile is calculated and the Gaisser-Hillas function (eqn. (3.1)) is fitted. The shower energy is derived from the calorimetric energy which is determined by the integral over the Gaisser-Hillas function and corrected for invisible energy (cf. sec. 3.3 and [19]). The depth of the shower maximum X_{max} is a direct result of the fit.

Cut	**Passed Events**		**Cumulated**
	absolute	relative	
All Data	89287	100 %	100 %
HEAT upward orientation	89287	100 %	100 %
Eye: Coihueco and/or HEAT	43728	49.0 %	49.0 %
Skip saturated pixels	43080	98.5 %	48.2 %
Skip bad pixels	43073	100 %	48.2 %
$E_{\mathrm{FD}} \geq 10^{15}$ eV	7703	17.9 %	8.63 %
Shower core is in SD array	7664	99.5 %	8.58 %
Min. 5 pixels for shower axis fit	6861	89.5 %	7.68 %
X_{max} in field of view	5138	74.9 %	5.75 %
$\sigma(X_{\mathrm{max}}) \leq 40\,\mathrm{g\ cm^{-2}}$	3071	59.8 %	3.44 %
$\sigma(E)/E \leq 20\%$	3042	99.1 %	3.41 %
Gaisser-Hillas χ^2/ndf ≤ 1.6	2902	95.4 %	3.25 %
Min. viewing angle $\geq 20°$	1968	67.8 %	2.20 %
Max. hole in depth profile $< 30\%$	1924	97.8 %	2.15 %
FD zenith angle $\leq 60°$	1902	98.9 %	2.13 %

(a) Coihueco and/or HEAT

Cut	**Passed Events**		**Cumulated**
	absolute	relative	
All Data	89287	100 %	100 %
HEAT upward orientation	89287	100 %	100 %
Eye: HEAT	33832	37.9 %	37.9 %
Skip saturated pixels	33257	98.3 %	37.2 %
Skip bad pixels	33257	100 %	37.2 %
$E_{\mathrm{FD}} \geq 10^{15}$ eV	4478	13.6 %	5.02 %
Shower core is in SD array	4430	98.9 %	4.96 %
Min. 5 pixels for shower axis fit	3537	79.8 %	3.96 %
X_{max} in field of view	2523	71.3 %	2.83 %
$\sigma(X_{\mathrm{max}}) \leq 40\,\mathrm{g\ cm^{-2}}$	1223	48.5 %	1.37 %
$\sigma(E)/E \leq 20\%$	1193	97.5 %	1.34 %
Gaisser-Hillas χ^2/ndf ≤ 1.6	1150	96.4 %	1.29 %
Min. viewing angle $\geq 20°$	571	49.7 %	0.64 %
Max. hole in depth profile $< 30\%$	565	98.9 %	0.63 %
FD zenith angle $\leq 60°$	558	98.8 %	0.62 %

(b) HEAT only

Table 4.1: Cuts applied on reconstructed air showers including the event selection efficiency for CoHe and HEAT with standard calibration. Further information on the used cuts can be found in [20].

5. Uncertainties on Parameters of the Shower Geometry

The analysis of the low-level shower parameters is presented based on the azimuth and zenith angle of the shower axis but is representative for all parameters of the shower geometry (cf. fig. 3.3). After the reconstruction of the selected data with standard calibration (std. cal.) and the changed HEAT calibration, the shower parameters of each event are read out and compared between the different calibrations. In the following, parameters gained from the reconstruction with modified calibration constants are marked with variables with a prime (e.g. φ') whereas parameters from a reconstruction with the standard calibration are marked without a prime (e.g. φ).

5.1 CoHe data

Fig. 5.1, 5.2, 5.3 and 5.4 exemplarily show the change of the azimuth and zenith angle due to the change of HEAT calibration constants by ± 1 and ± 5 standard deviations with CoHe data. For ± 3 σ and ± 10 σ, the plots can be found in the Appendix A as they are very similar to the plots presented in this section. Due to the fact, that depending on the calibration, different events are selected by the cuts, the number of events in the histograms is not constant. Only if an event is selected with the standard calibration as well as with the changed calibration, a comparison between both is possible.

It is important to note that the y-axis in the histograms is logarithmic. Therefore for nearly all events, the change of the HEAT calibration has no effect on the shower geometry within the binning of the histograms. The bin size of the histograms is 0.1° whereas the angular resolution of the Pierre Auger Observatory is about 1° and only single events show a deviation of $|\varphi' - \varphi| > 1°$. These events are EAS with a very small zenith angle. The shower axis of an EAS with a small zenith angle is nearly vertical which leads to a high uncertainty in the determination of the azimuth angle. The outlier event in fig. 5.2a with $\varphi' - \varphi \approx -8°$, for instance, has an zenith angle of $\theta = 5°$ and an uncertainty on the azimuth angle of $\sigma_{\text{azimuth}} = 14°$. To take into account that for small zenith angle, the azimuth angle has only a small influence on the orientation of the shower axis, the angular distance of the reconstructed shower axes is exemplarily shown in fig. 5.5. It can be seen that for all events, the angular distance between the shower axes is smaller than 1° and therefore within the resolution and more than 99 % of the events are included in the bin between 0° and 0.1°.

Additionally, the change of the shower geometry seems to be independent of the direction of the change of the calibration constants. The mean of all histograms is compatible with zero and no mirroring of events at zero is found by the comparison of e.g. fig. 5.1a and fig. 5.1b.

One can conclude that the change of the shower geometry stays within the resolution of the detector and therefore, uncertainties on the HEAT calibration have no significant impact on the reconstruction of the shower geometry. But although the change of the shower geometry is relatively small, the reasons for these changes are not understood yet. As the geometry reconstruction uses mainly the timing information of the FD pixels (cf. sec. 3.3) a change of the calibration constants is not supposed to change this reconstruction. While the charge of each pixel is used as well as a weighting factor in the fit (cf. [23]), this charge is the integral of ADC counts of each pixel[24] and therefore not changed by calibration constants.

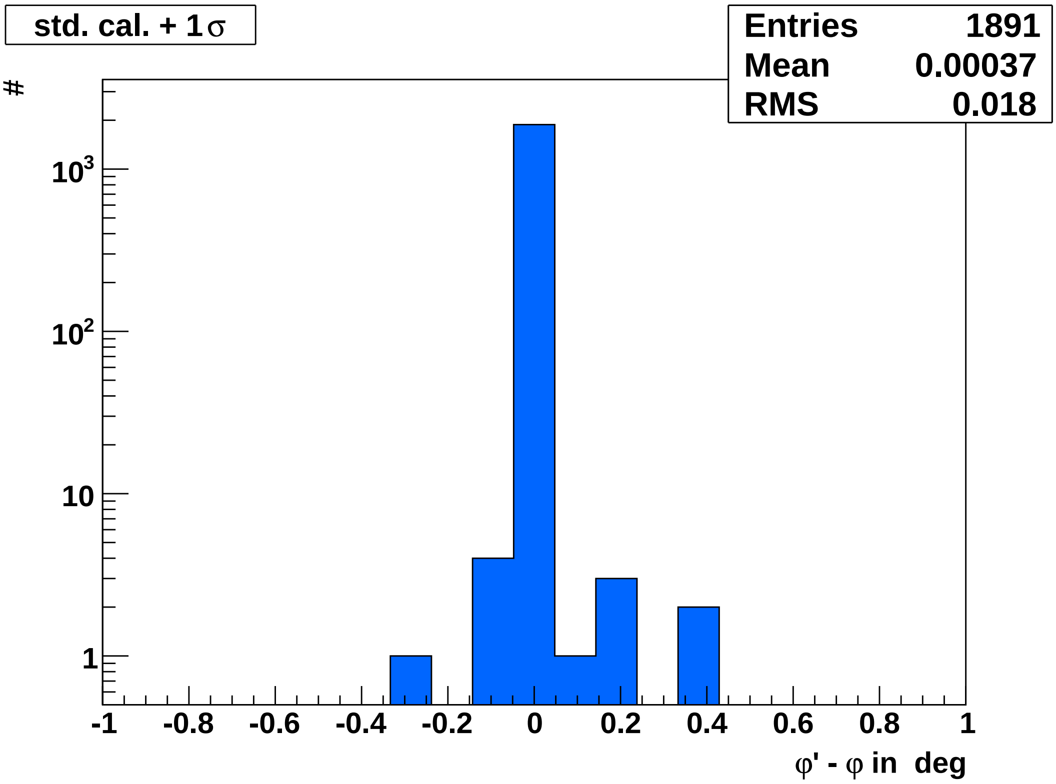

(a) HEAT standard calibration + 1 standard deviations

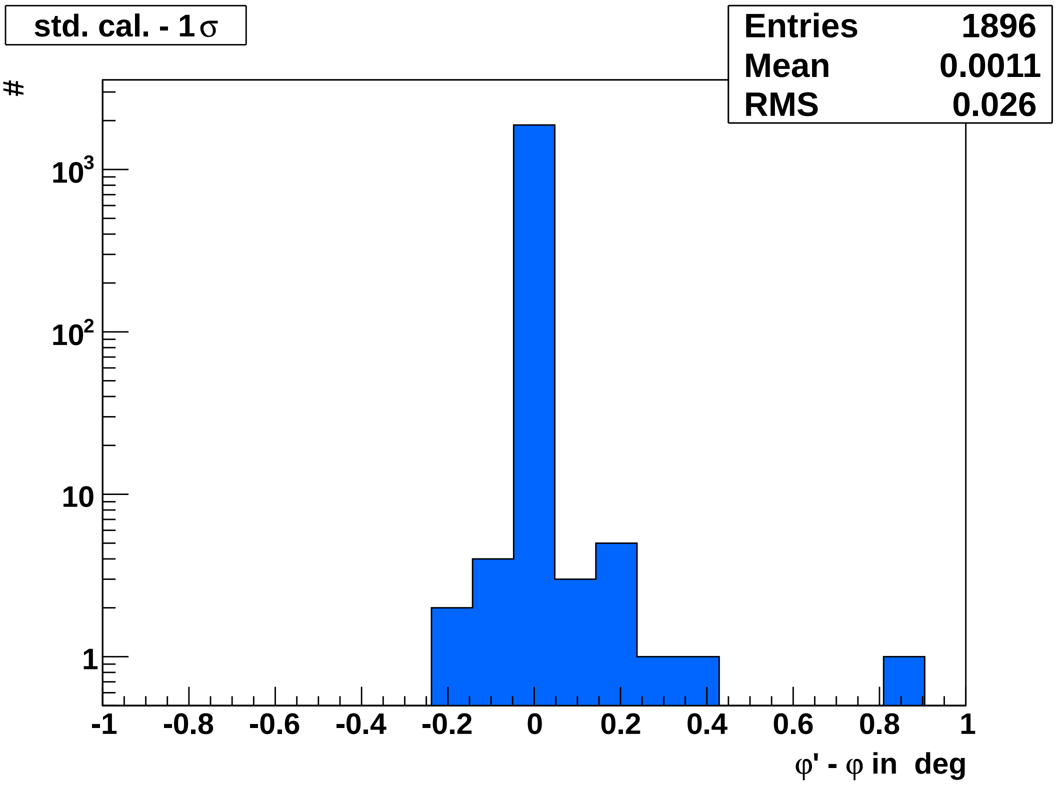

(b) HEAT standard calibration - 1 standard deviations

Figure 5.1: Histogram of the change of the azimuth angle of the reconstructed shower axis due to the change of the HEAT calibration constants by ± 1 standard deviations. φ is the shower azimuth reconstructed with standard calibration whereas φ' is the azimuth reconstructed with changed calibration constants.

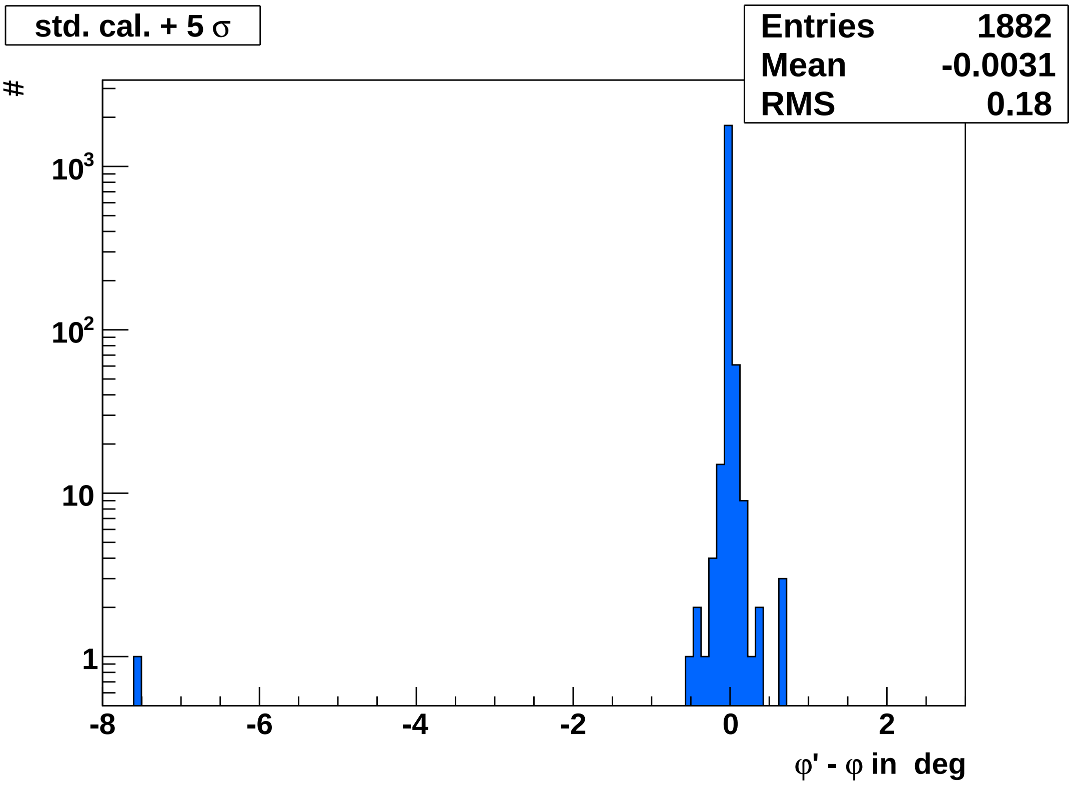

(a) HEAT standard calibration + 5 standard deviations

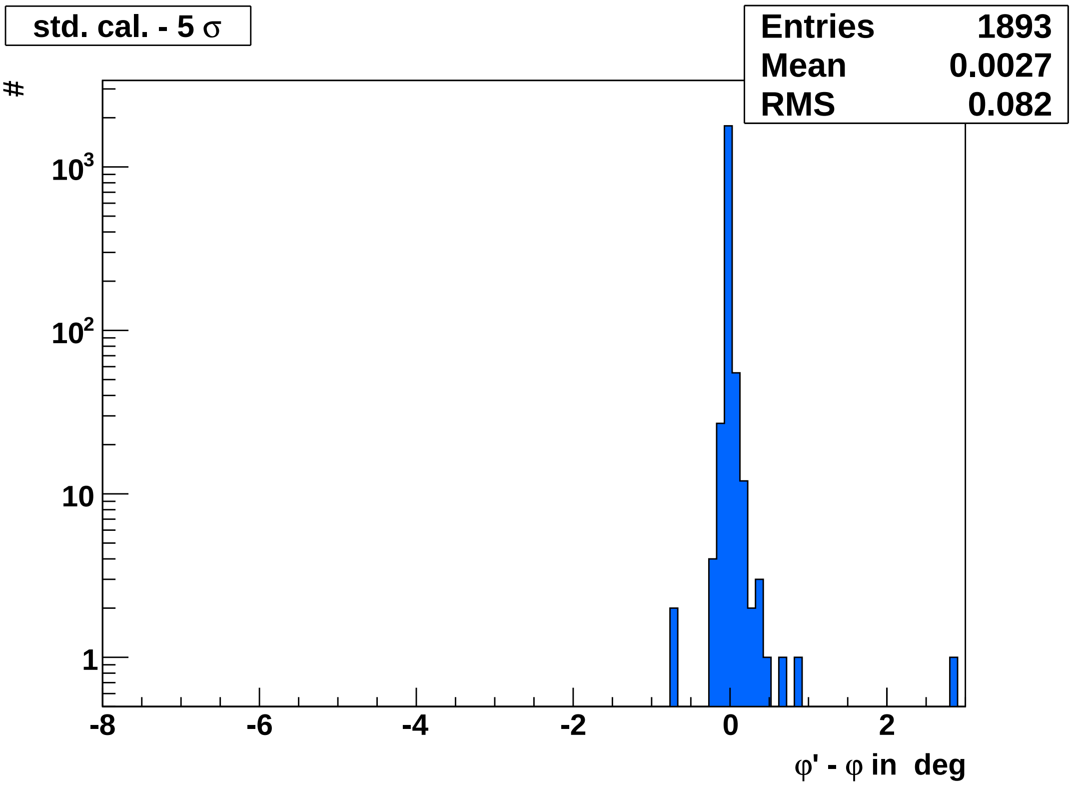

(b) HEAT standard calibration - 5 standard deviations

Figure 5.2: Histogram of the change of the azimuth angle of the reconstructed shower axis due to the change of the HEAT calibration constants by ± 5 standard deviations. φ is the shower azimuth reconstructed with standard calibration whereas φ' is the azimuth reconstructed with changed calibration constants.

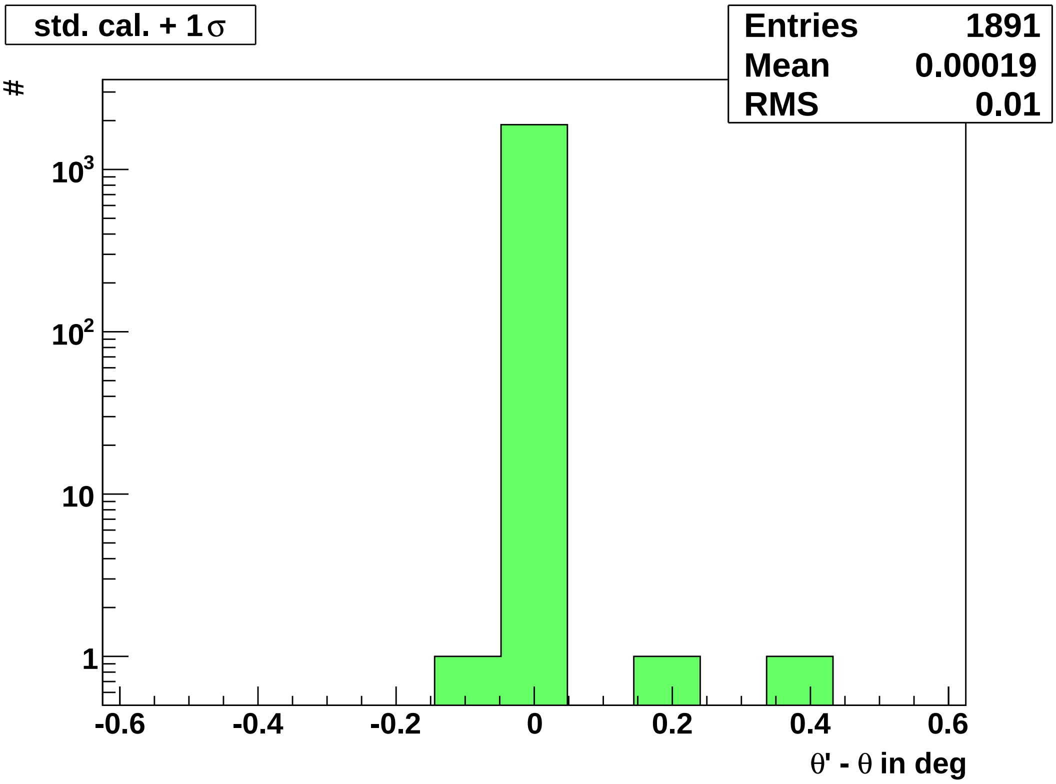

(a) HEAT standard calibration + 1 standard deviations

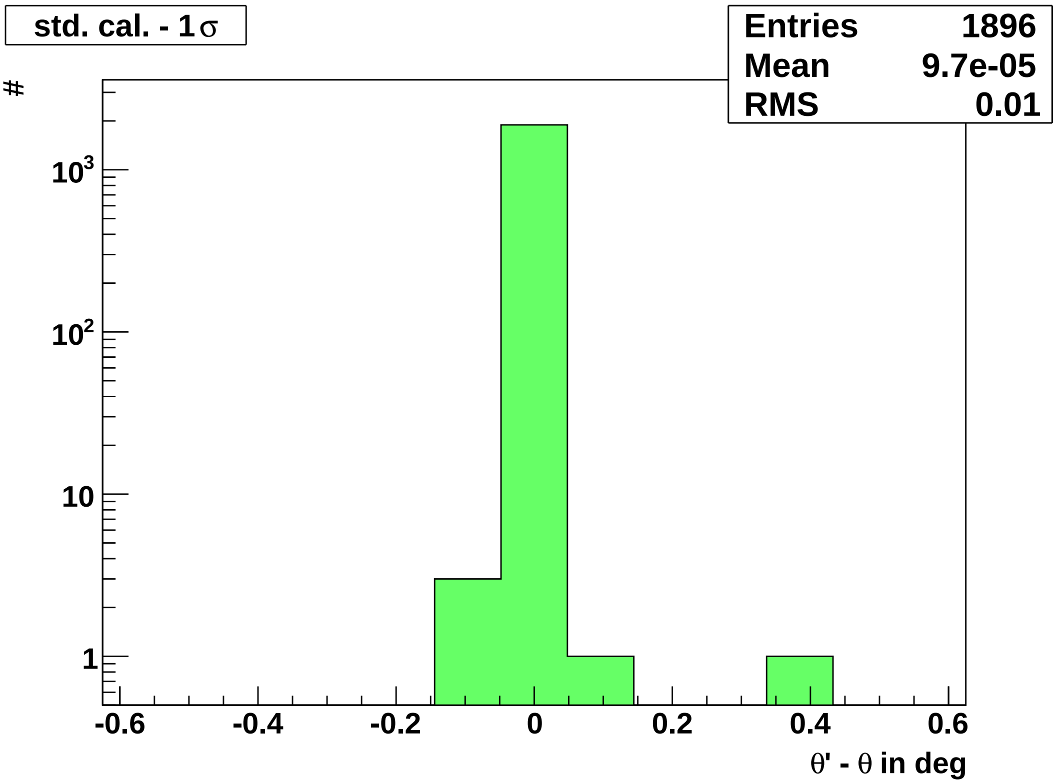

(b) HEAT standard calibration - 1 standard deviations

Figure 5.3: Change of zenith of the reconstructed shower axis due to the change of the HEAT calibration constants by ± 1 standard deviations. θ is the shower zenith reconstructed with standard calibration whereas θ' is the zenith reconstructed with changed calibration constants.

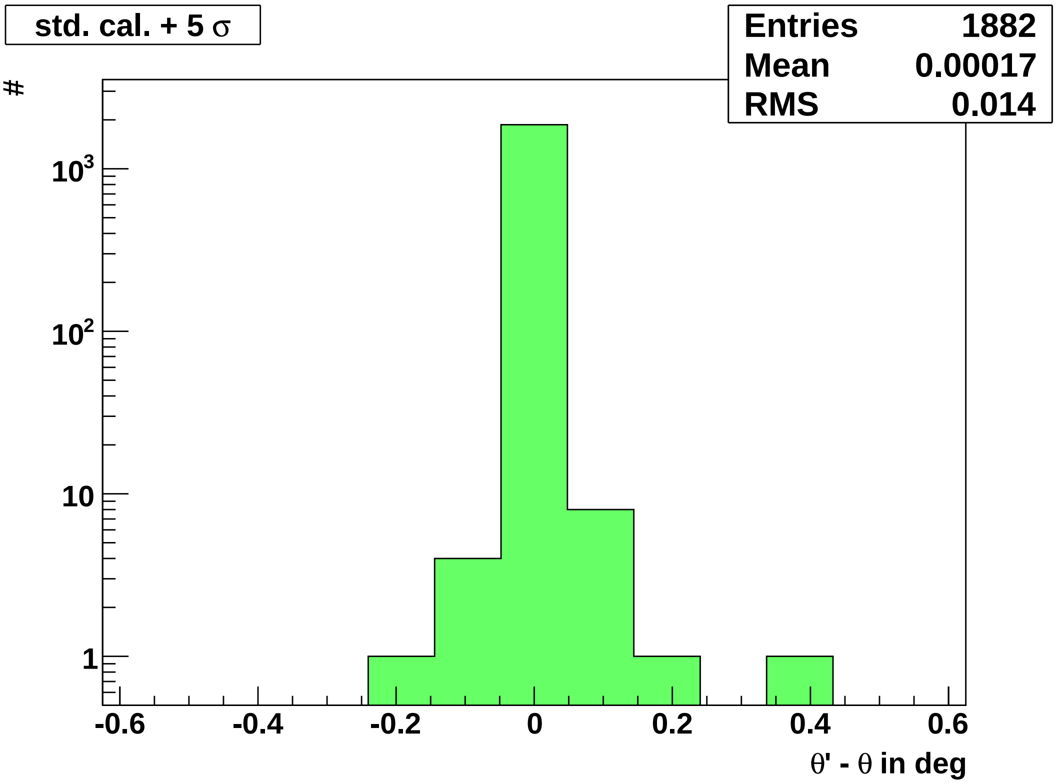

(a) HEAT standard calibration + 5 standard deviations

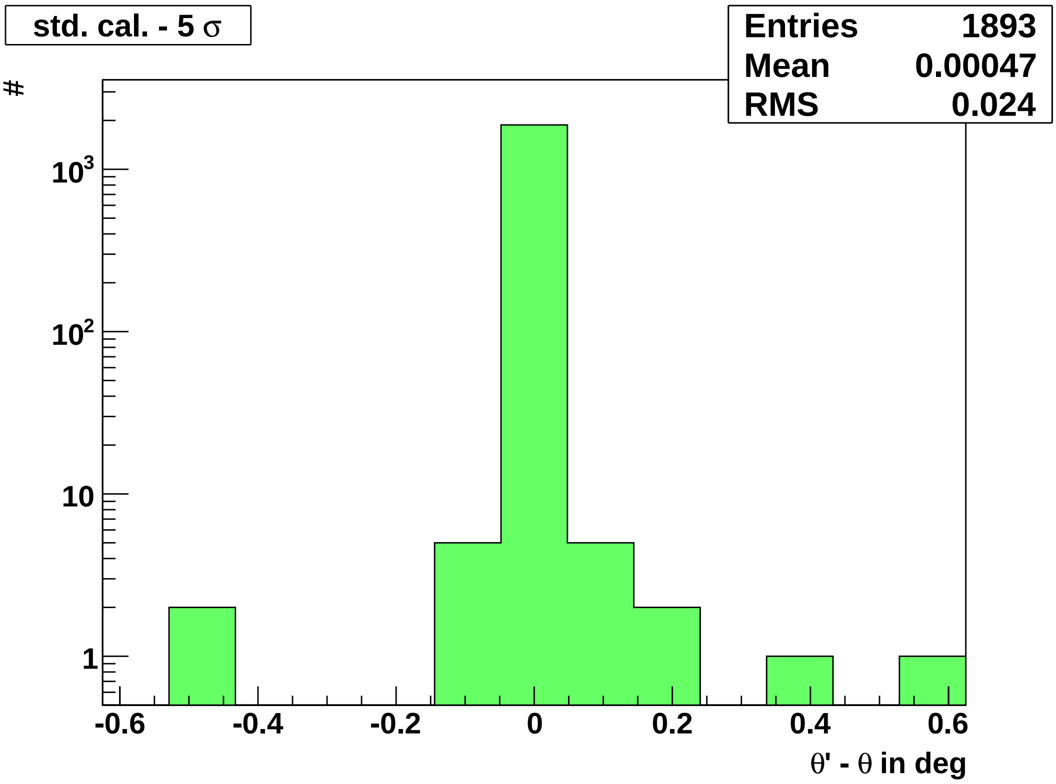

(b) HEAT standard calibration - 5 standard deviations

Figure 5.4: Change of zenith of the reconstructed shower axis due to the change of the HEAT calibration constants by ± 5 standard deviations. θ is the shower zenith reconstructed with standard calibration whereas θ' is the zenith reconstructed with changed calibration constants.

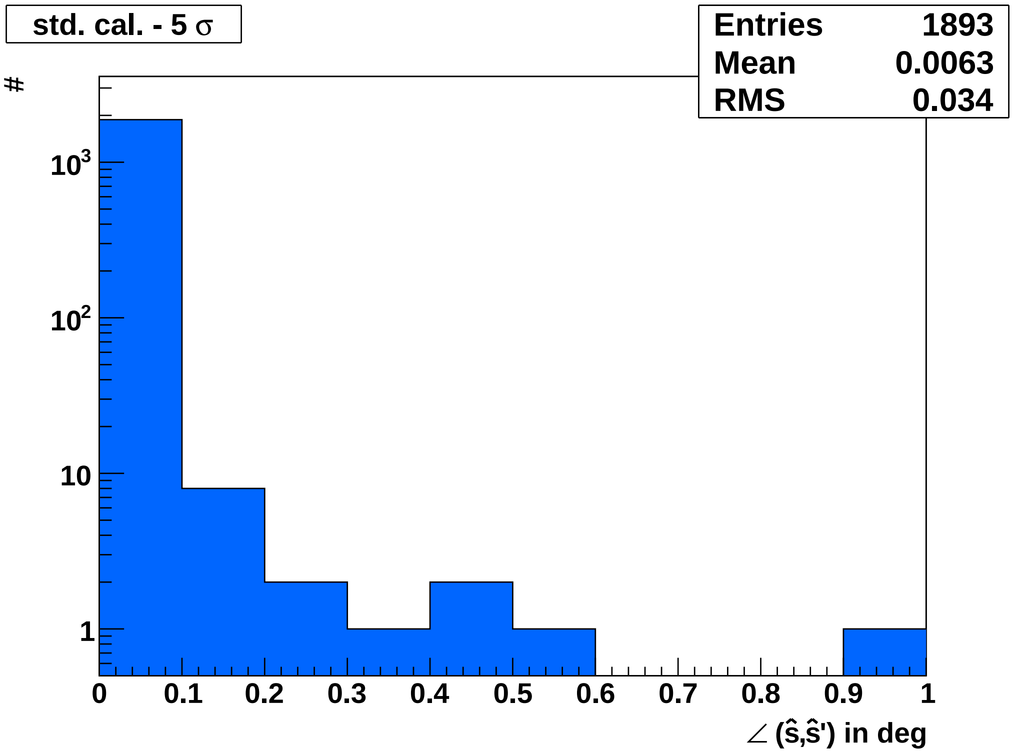

Figure 5.5: Histogram of the angular distance between reconstructed shower axes of reconstructions with standard calibration and changed HEAT calibration.

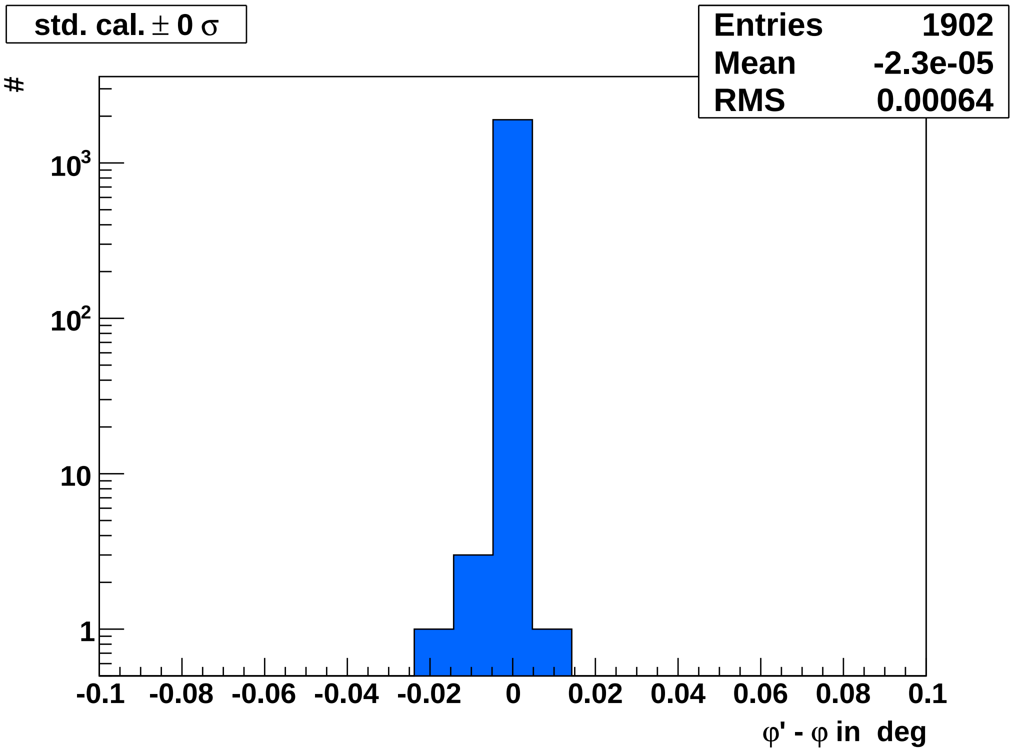

Figure 5.6: Comparison of two reconstructions of the same data set using the same (standard) calibration. φ' and φ are the azimuth angles of the two reconstructions. The bin size is only 1/10 (0.01°) of the one used in the former histograms.

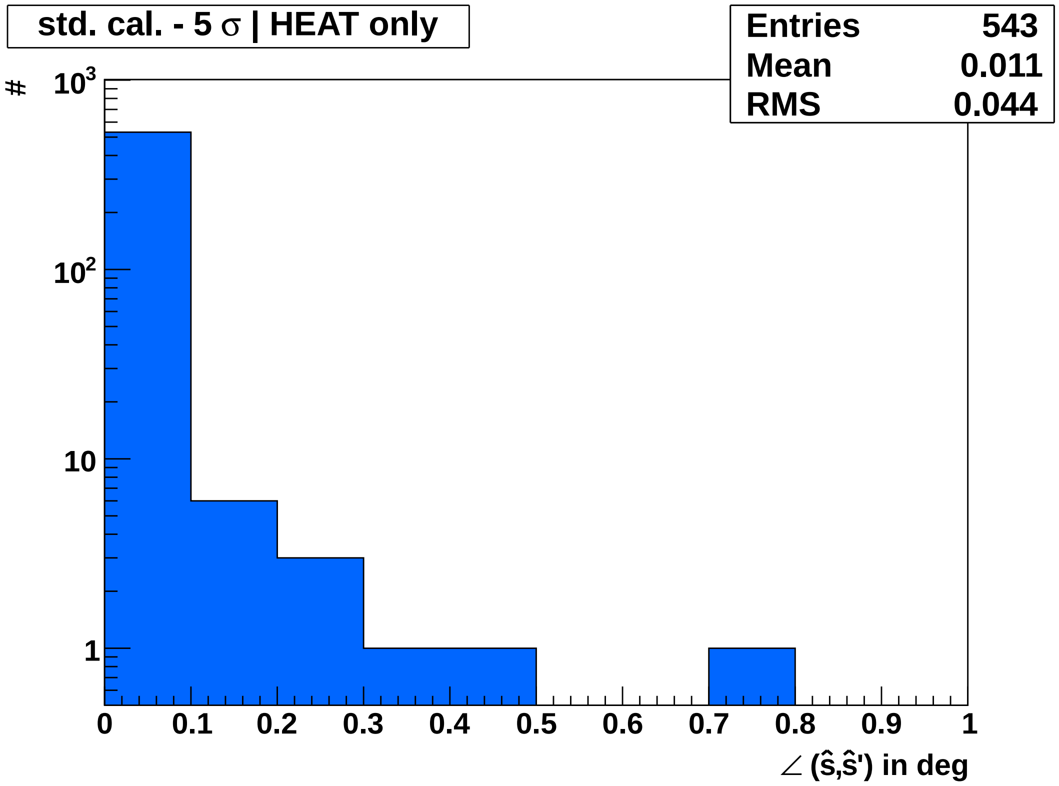

Figure 5.7: Angular distance between reconstructed shower axes of reconstructions with standard calibration and changed HEAT calibration with HEAT only data.

One possible reason for these changes are the random number generators used for the fits in the reconstruction. This may lead to fluctuations in the reconstruction of the same shower independent of the calibration constants. To check whether this effect could explain these kind of geometry changes, the chosen data set was reconstructed again using the standard calibration. Fig. 5.6 show the results of this second reconstruction based on the azimuth angle. A smaller binning was chosen since otherwise the bin around 0 would contain all entries. This shows that there are indeed small fluctuations in the reconstruction of the same shower but they are not able to explain the changes found with changed HEAT calibration constants.

5.2 HEAT data

The analysis described in this chapter is also applied on data measured with HEAT only. Fig. 5.7 is again exemplarily for all changes of the HEAT calibration and shows that the same effect is found in HEAT-only data. Therefore, this effect is not caused by the combined reconstruction of events seen by HEAT and Coihueco either.

6. Uncertainties on Energy and Depth of the Shower Maximum

As the reconstruction of the shower energy E or the depth of the shower maximum X_{max} requires several complex physical models, like the production of Cherenkov light or the scattering of light in the air, these parameters are referred to as high-level parameters. The number of photons emitted from the EAS and detected by the FD is proportional to the energy deposited in the atmosphere [25]. Therefore, a linear correlation between the change of calibration constants and the change of the reconstructed energy is expected. Due to the fact, that the energy of each pixel is increased or decreased uniformly with the change of the calibration constants, no change of the detected maximum of the energy deposit, and therefore X_{max}, is expected. Nevertheless, for events which were observed by HEAT and Coihueco, there may be a shift of X_{max} as the calibration constants of Coihueco are untouched. The raise/lowering of the HEAT data points can lead to a new maximum in the longitudinal shower profile and thus to a new X_{max}. For a better understanding of the impact of changing the HEAT calibration on the high-level parameters, the effect on HEAT-only data is studied first.

6.1 HEAT data

6.1.1 Shower Energy

Fig. 6.1 shows the relative change of the reconstructed energy depending on the change of HEAT calibration constants and the energy of the showers. For each energy bin (bin size 0.25 decades) the arithmetical mean μ and the uncertainty of the mean

$$\sigma_\mu = \frac{1}{\sqrt{N}}\sqrt{\frac{1}{N-1}\sum_{i=1}^{N}(x_i-\mu)^2} = \frac{\sigma}{\sqrt{N}} \tag{6.1}$$

is calculated. Although the event reconstruction calculates an uncertainty for the energy of each event, these uncertainties can not be used for the calculation of an weighted mean as those of E and E' are strongly correlated but the exact correlation is unknown. The event numbers below the data points are those for a change of a HEAT calibration of + 1 standard deviation. Due to the selection of different events by the cuts (cf. sec. 5.1) these numbers may vary by ± 6 events for bins with > 30 entries for the different calibrations. In the Appendix B the number of events for each change of the calibration constants can be found.

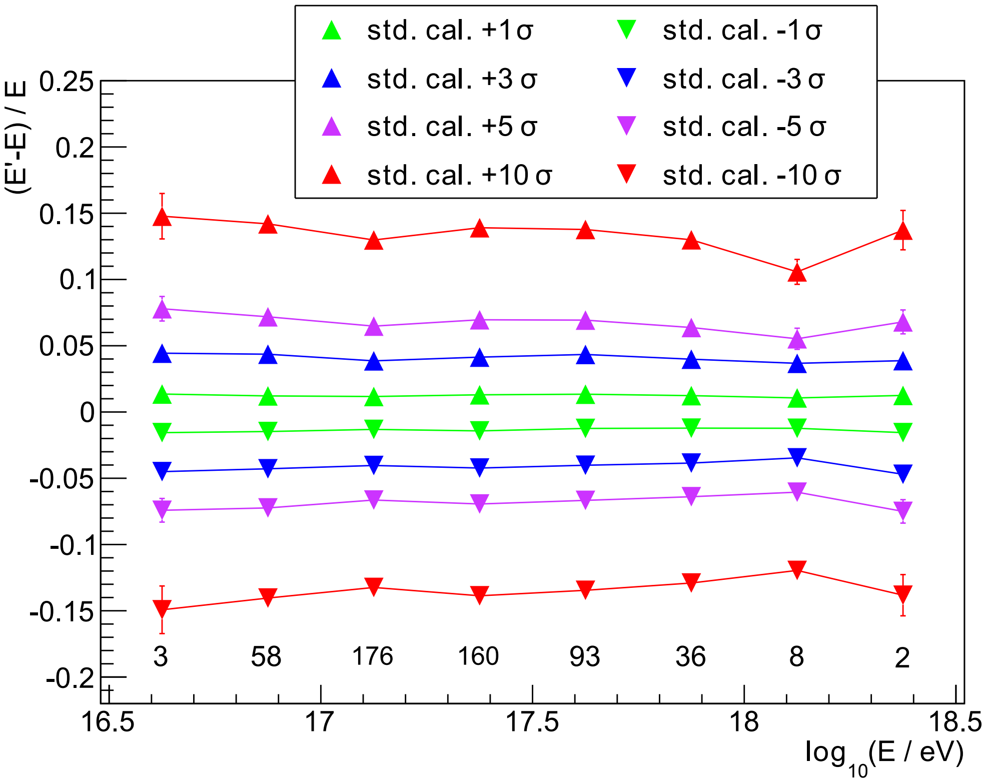

Figure 6.1: Relative change of the reconstructed shower energy depending on the change of HEAT calibration constants and the shower energy with HEAT-only data. E is the shower energy reconstructed with standard calibration whereas E' is the energy reconstructed with changed calibration constants. The data points show the mean values of the events of the respective calibration and energy bin and the uncertainties are given by the uncertainties of the mean. The numbers below the data points are the number of events in the particular energy bin.

As expected, an increase/decrease of the HEAT calibration constants leads to an increase/decrease of the reconstructed energy independent of the energy of the shower itself. As a change of the calibration of 1 standard deviation corresponds to a change of the calibration constants of about 1.3 % one can see that the relative change of calibration and energy is at the same level. For a further quantitative analysis of the change of the energy a constant is fitted with a χ^2 minimization on each graph in fig. 6.1. The results are found in tab. 6.1.

While most of the χ^2-values seem a bit high in comparison to the number of degrees of freedom they are still in agreement with a χ^2 distribution. Anyway, this may be an indication that the uncertainties assumed by eqn. (6.1) are too small. As a linear correlation between the change of the calibration constants and the relative change

Δ cal. const. / σ_{cal}	relative change of energy / 10^{-2}	χ^2/ndf
+ 10	13.38 ± 0.14	$15.9/7 \approx 2.3$
+ 5	6.75 ± 0.08	$16.1/7 \approx 2.3$
+ 3	4.09 ± 0.06	$13.8/7 \approx 2.0$
+ 1	1.26 ± 0.03	$7.1/7 \approx 1.0$
- 1	-1.37 ± 0.02	$18.3/7 \approx 2.6$
- 3	-4.12 ± 0.05	$12.3/7 \approx 1.8$
- 5	-6.77 ± 0.07	$15.5/7 \approx 2.2$
- 10	-13.44 ± 0.12	$12.3/7 \approx 1.8$

Table 6.1: Results of the fits of a constant c on the graphs in fig. 6.1.

of energy is expected, a straight line without y-intercept[1] is fitted on the "relative change" values in tab. 6.1:

$$\frac{E' - E}{E} = m \cdot \frac{\Delta\text{cal. const.}}{\sigma_{\text{cal}}} \tag{6.2}$$

The result of the fit is

m / 10^{-2}	χ^2/ndf
1.349 ± 0.006	$12.1/7 \approx 1.7$

So the change of the HEAT calibration constants by 1 standard deviation results in a relative change of the reconstructed shower energies of 1.349 %. As 1 standard deviation of the three HEAT calibration constants corresponds on average to 1.339 % of the calibration constants, this result is consistent with the expectation.

6.1.2 Depth of the Shower Maximum

Fig. 6.2 shows analogue to fig. 6.1 the change of the depth of the shower maximum X_{max} depending on the change of HEAT calibration constants and the shower energy. As one can see there is no systematic change of X_{max} in HEAT-only data with the change of the calibration constants and all data points are consistent with zero within their uncertainties. To compare the change of X_{max} in absolute values: EAS with a shower maximum seen by HEAT have an X_{max} of about $600 - 800\,\text{g cm}^{-2}$. Therefore, the absolute change of the X_{max} in fig. 6.2 is less than $8\,\text{g cm}^{-2}$ while the resolution of X_{max} of the FD is about $40\,\text{g cm}^{-2}$.

---

[1] for no change of the calibration constants there is no change of the reconstructed energy

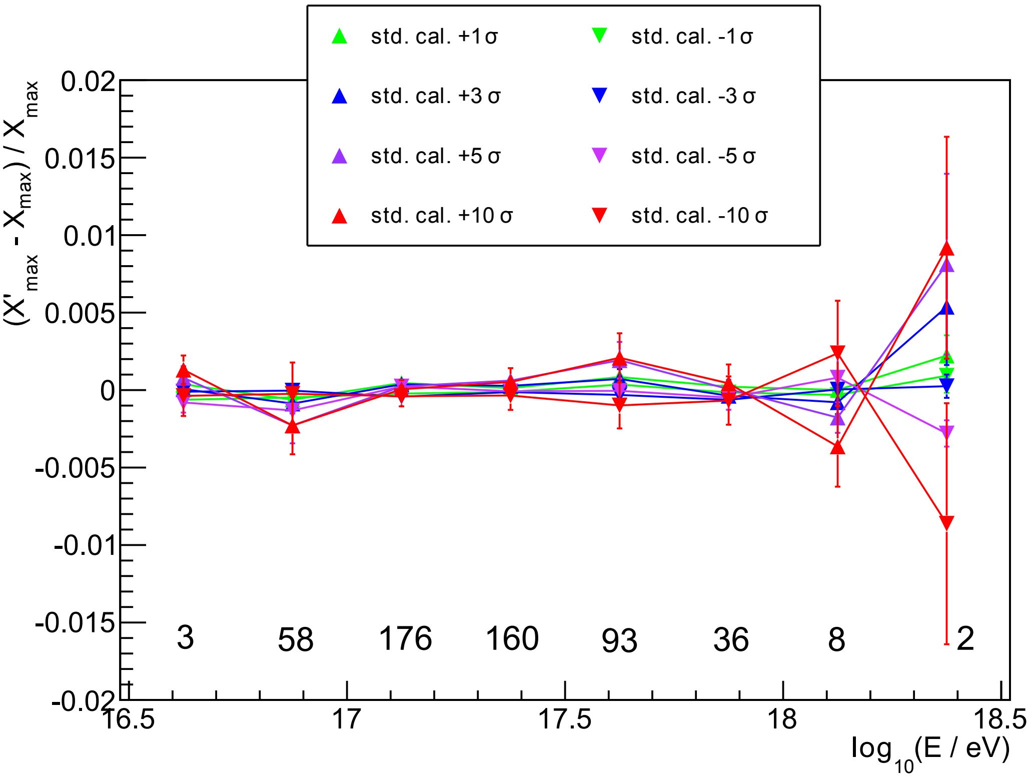

Figure 6.2: Relative change of the reconstructed depth of the shower maximum X_{max} depending on the change of HEAT calibration constants and the shower energy with HEAT-only data. X_{max} is the depth of the shower maximum reconstructed with standard calibration whereas X'_{max} is the depth of the shower maximum reconstructed with changed calibration constants. The data points show the mean values of the events of the respective calibration and energy bin and the uncertainties are given by the uncertainties of the mean. The numbers below the data points are the number of events in the particular energy bin.

6.2 CoHe data

6.2.1 Shower Energy

Fig. 6.3a shows the relative change of the reconstructed energy depending on the change of HEAT calibration constants and the energy of the showers with CoHe data. In contrast to HEAT-only data (cf. fig. 6.1), the change of the energy shows a systematic dependence on the shower energy: The higher the energy of the EAS is, the smaller the impact of changed HEAT calibration constants on energy reconstruction is. As HEAT is designed to detect lower energy showers in lower atmospheric depths (cf. sec. 3.4) the contribution of HEAT to the reconstruction of EAS decreases towards higher energies in the virtual CoHe eye (cf. Appendix C on page 45). Conversely, the contribution of Coihueco increases with higher energies. Due to the fact that the Coihueco calibration constants are untouched, no energy change for showers or shower parts seen by Coihueco is expected. Therefore the changes in fig. 6.3a meet the expectations: For showers with low energies, which are mainly

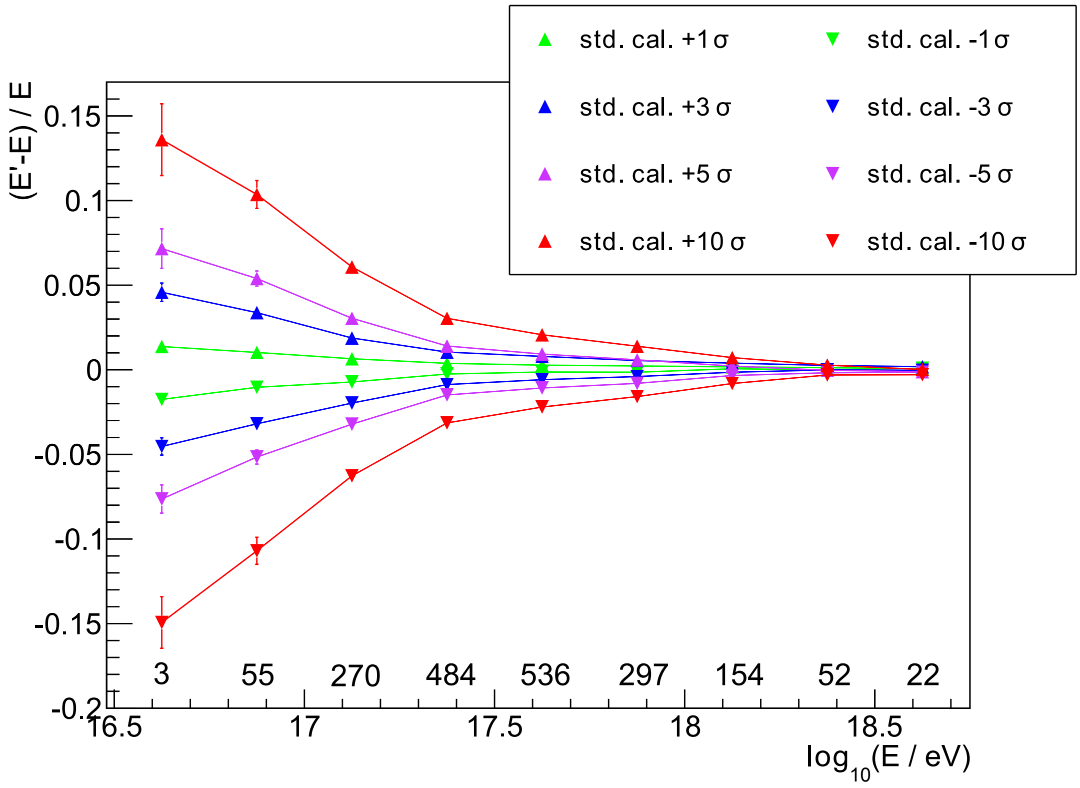

(a) Relative change of energy

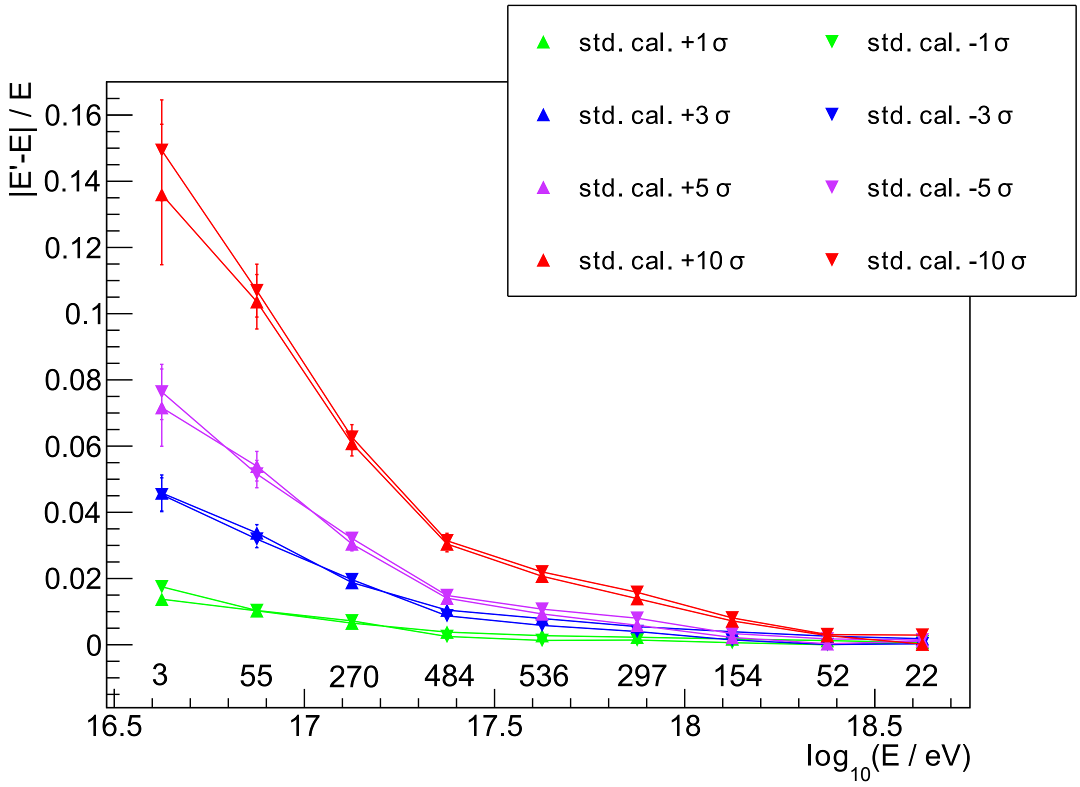

(b) Absolute values of the relative change of energy

Figure 6.3: Relative change of the reconstructed shower energy depending on the change of HEAT calibration constants and the shower energy with CoHe data. E is the shower energy reconstructed with standard calibration whereas E' is the energy reconstructed with changed calibration constants. The data points show the mean values of the events of the respective calibration and energy bin and the uncertainties are given by the uncertainties of the mean. The numbers below the data points are the number of events in the particular energy bin (cf. tab. B.2).

seen by the HEAT telescopes, the impact on the reconstructed energy is as high as described in section 6.1.1 for HEAT-only data. For increasing energies, the fraction of the longitudinal shower profile seen by Coihueco increases as well, lowering the effect of changed HEAT calibration constants on the event reconstruction. Thus, the relative change of the reconstructed energy is lowered as well until it is zero for high energy EAS detected completely by Coihueco.

To check whether the change of the calibration constants in one direction has a greater influence on the reconstruction than in the other direction, fig. 6.3b shows the absolute values of the change of the reconstructed shower energy. As one can see, the data points for an increased and decreased HEAT calibration are in agreement within the uncertainties.

6.2.2 Depth of the Shower Maximum

As can be seen from fig. 6.4a the change of HEAT calibration constants has also a systematic impact on the reconstruction of the depth of the shower maximum X_{max}. Especially for energies between 10^{17} and 10^{18} eV, a decrease of the calibration of the HEAT telescopes leads to an increase of the reconstructed X_{max} and vice versa. Yet, this effect is not significant as CoHe measures EAS with an X_{max} of up to $1000\,\mathrm{g\,cm^{-2}}$ and therefore a deviation of 2 % is still within the resolution of about $40\,\mathrm{g\,cm^{-2}}$. The systematic change of X_{max} can be explained with the fact that the calibration constants of Coihueco are untouched, which is able to lead to a shift of the reconstructed shower maximum. Fig. 6.5 illustrates this effect. While this is an extreme example it clarifies the impact of changing the calibration of only one of the eyes used in the combined reconstruction in the virtual CoHe eye.

Fig. 6.4b compares the influence of an increased and decreased HEAT calibration on X_{max} by showing the absolute values of the relative change of the depth of the shower maximum. It shows that, especially for ± 5 and ± 10 standard deviations, the lowering of the HEAT calibration constants has an higher impact on the reconstruction of X_{max} than the raising. The reason for this lack of symmetry cannot be clarified within this work. One reason could be that HEAT observes more showers close to the telescopes (cf. sec. 3.4.1). Hence, many of the EAS seen by HEAT hit the ground behind HEAT and therefore outside of the SD array. As this work is based on hybrid data[2], these showers are not analysed. This leads to more showers with an higher ratio of Coihueco data points within the CoHe reconstruction which may distort the analysis. Further analyses (e.g. including Monte Carlo simulations) are needed for a final explanation of this asymmetry.

---

[2] atleast one triggered SD station is needed

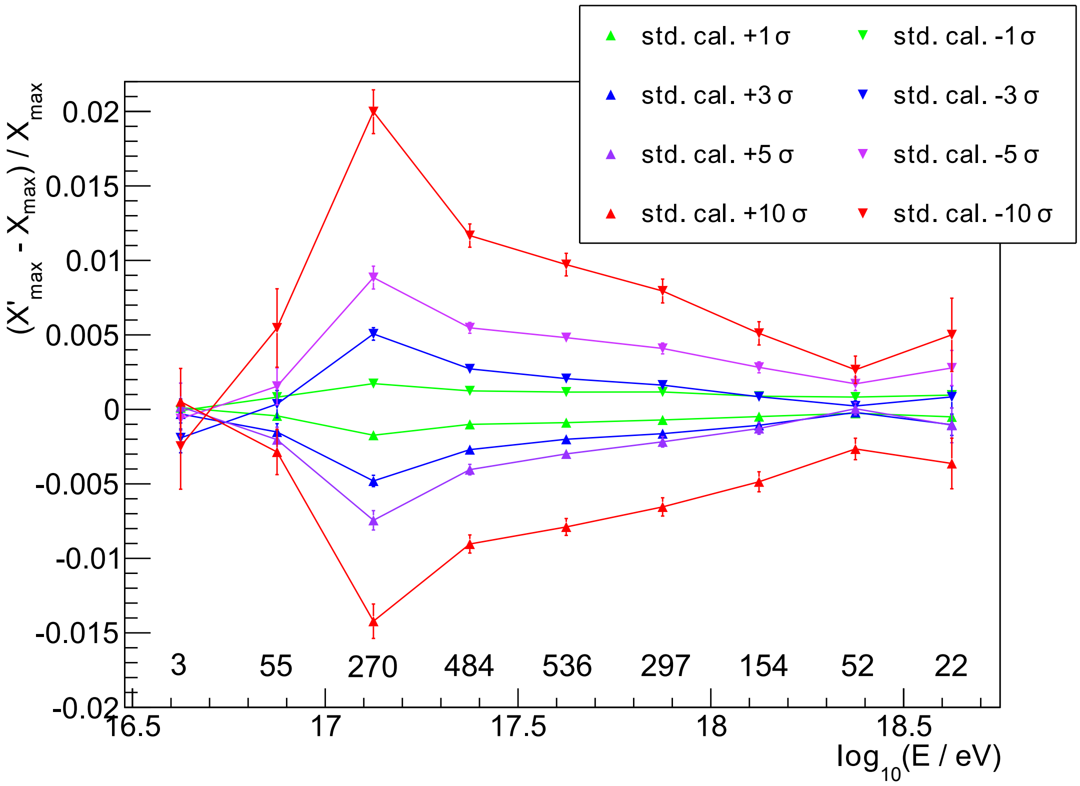

(a) Relative change of the shower maximum $X_{\max}$

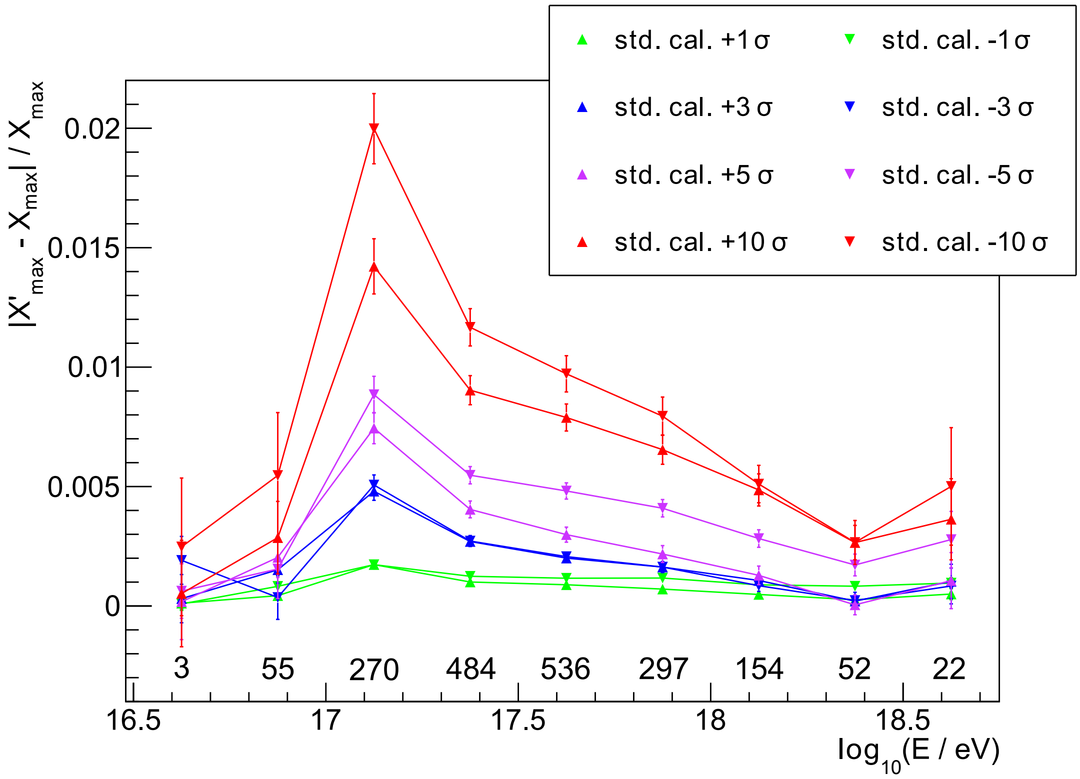

(b) Absolute values of the relative change of the shower maximum $X_{\max}$

Figure 6.4: Relative change of the reconstructed depth of the shower maximum $X_{\max}$ depending on the change of HEAT calibration constants and the shower energy with CoHe data. $X_{\max}$ is the depth of the shower maximum reconstructed with standard calibration whereas $X'_{\max}$ is the depth of the shower maximum reconstructed with changed calibration constants. The data points show the mean values of the events of the respective calibration and energy bin and the uncertainties are given by the uncertainties of the mean. The numbers below the data points are the number of events in the particular energy bin (cf. tab. B.2).

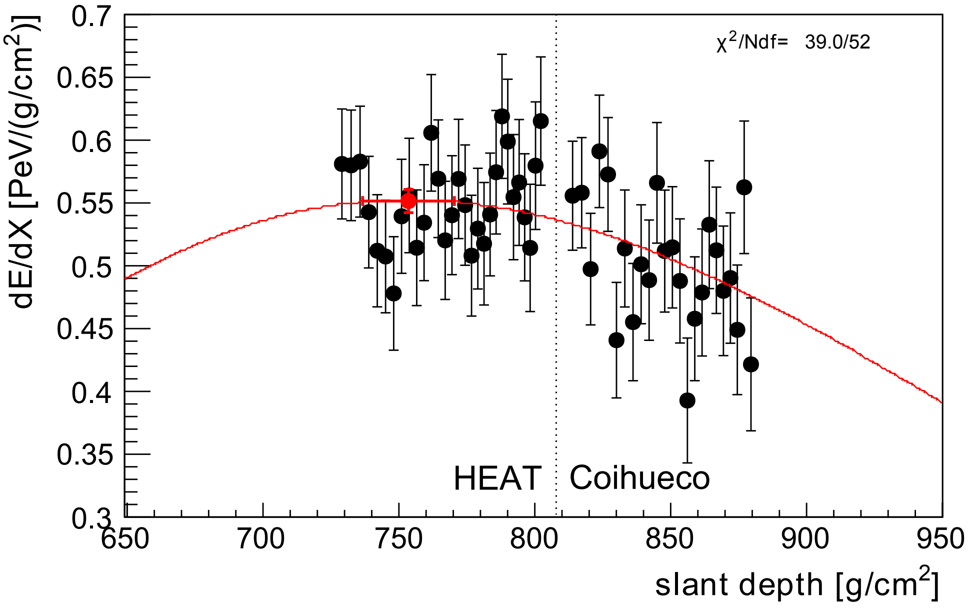

(a) standard calibration

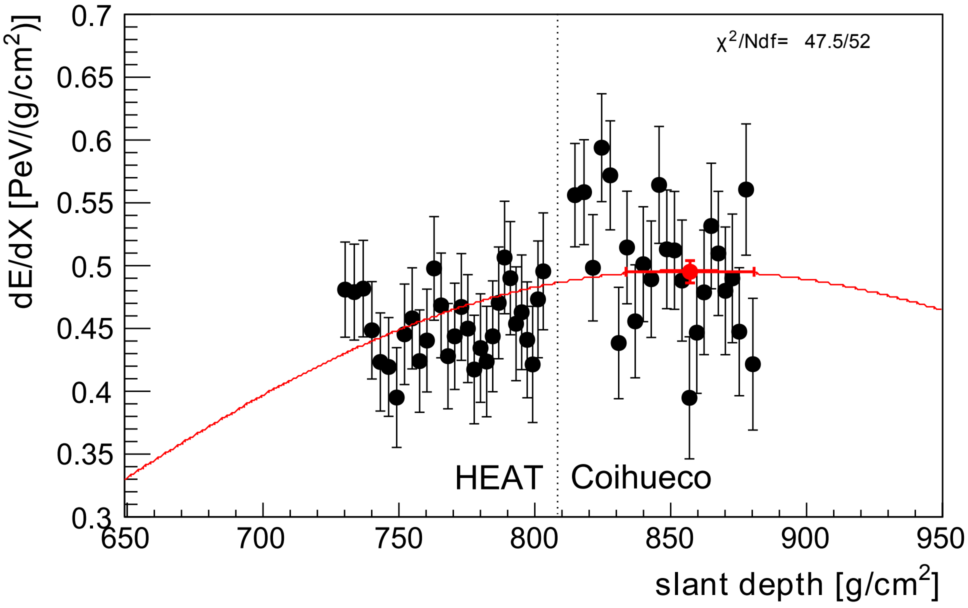

(b) HEAT calibration - 10 σ, Coihueco calibration unchanged

Figure 6.5: Shift of the reconstructed X_{max} due to the change of HEAT calibration constants. (a) shows the longitudinal shower profile of a $3.5 \cdot 10^{17}$ eV EAS (SD Event ID 10189377) reconstructed with standard HEAT and Coihueco calibration constants. In (b) the same shower is reconstructed with a HEAT calibration decreased by 10 σ. The red line represents the fitted Gaisser-Hillas function and the red dot the maximum of the function including its uncertainties. As Coihueco looks at higher atmospheric depths, the decrease of the HEAT calibration increases the reconstructed X_{max}.

7. Conclusion and Outlook

The analysis presented here is based on data taken with the fluorescence detector site Coihueco and the low energy extension HEAT at the Pierre Auger Observatory in Argentina. The field of view of the telescopes of Coihueco and HEAT are complementary, allowing a combined observation of extensive air showers, induced by cosmic ray particles. The impact of the uncertainties of the preliminary HEAT calibration on the reconstruction of HEAT-only and combined Coihueco and HEAT (CoHe) data was analysed based on the reconstruction of the shower geometry, the shower energy and the depth of the shower maximum X_{max}.

The study of the shower geometry showed that the uncertainties of the HEAT calibration constants have no significant effect on the reconstruction of geometry parameters. Nevertheless, a small change of the shower geometry were found which cannot be explained by fluctuations in the reconstruction of the same shower.

As the calibration constants have a direct influence on the reconstruction of the shower energy, a strong correlation between the varying of the calibration and the change of the reconstructed shower energy was expected and found. For HEAT-only data, the energy changes in the exact same ratio as the calibration is altered, which allowed a parametrisation of the change of shower energy depending on the change of the HEAT calibration. The analysis of CoHe data showed that the change of energy is depending on the energy of the shower itself and therefore on the proportion of HEAT pixels involved in the CoHe analysis, as the Coihueco calibration was untouched.

Varying the HEAT calibration constants within their uncertainties has no impact on the depth of the shower maximum X_{max} for data reconstructed with HEAT only, as all data points are raised/lowered uniformly. For CoHe data, an increase of the constants of the HEAT calibration leads to a small decrease of the reconstructed X_{max} and vice versa as the shower maximum may shift in the field of view of the other detector site and therefore to lower or higher atmospheric depths.

Outlook

The approach for this work was to uniformly raise or lower all three HEAT calibration constants which allowed to systematically analyse the effect on the event reconstruction. The next step is to change the calibration constants independently. One possible ansatz is to change the constants randomly by applying a Gaussian distribution with the respective mean value and standard deviation on each constant to simulate a more likely scenario. Even after the implementation of the final absolute calibration of the HEAT telescopes, which is planned for the end of 2012, this could be performed on the calibration constant of each pixel. Such an analysis may include a deeper look at the correlation between shower parameters reconstructed with different calibration constants, allowing a better estimation of the respective uncertainties.

The analysis of the absolute values of the change of the shower maximum X_{max} showed an asymmetry between lowering and raising the HEAT calibration constants. Lowering the calibration seems to have an higher impact on the reconstruction of X_{max} than the raising. This may be caused by the fact that this work is based on events not only seen by the fluorescence detector but also by the surface detector of the Pierre Auger Observatory. As many HEAT events are not detected by the surface detector, this could lead to a distortion of the analysis. Further analyses including Monte Carlo simulations may explain this asymmetry.

Additionally, the change of the shower geometry due to the change of the HEAT calibration constants is not fully understood yet and may require further studies.

A. Change of Shower Geometry

A.1 Azimuth

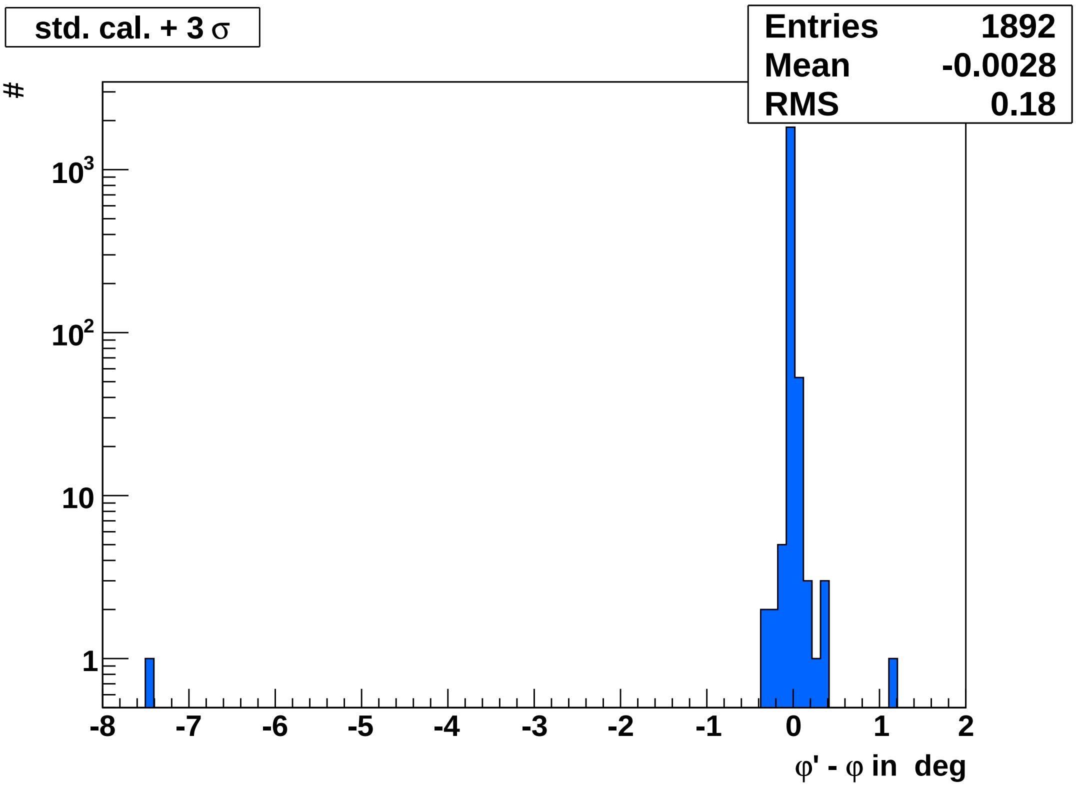

Figure A.1: Histogram of the change of the azimuth angle of the reconstructed shower axis due to the change of the HEAT calibration constants by + 3 standard deviations. φ is the shower azimuth reconstructed with standard calibration whereas φ' is the azimuth reconstructed with changed calibration constants.

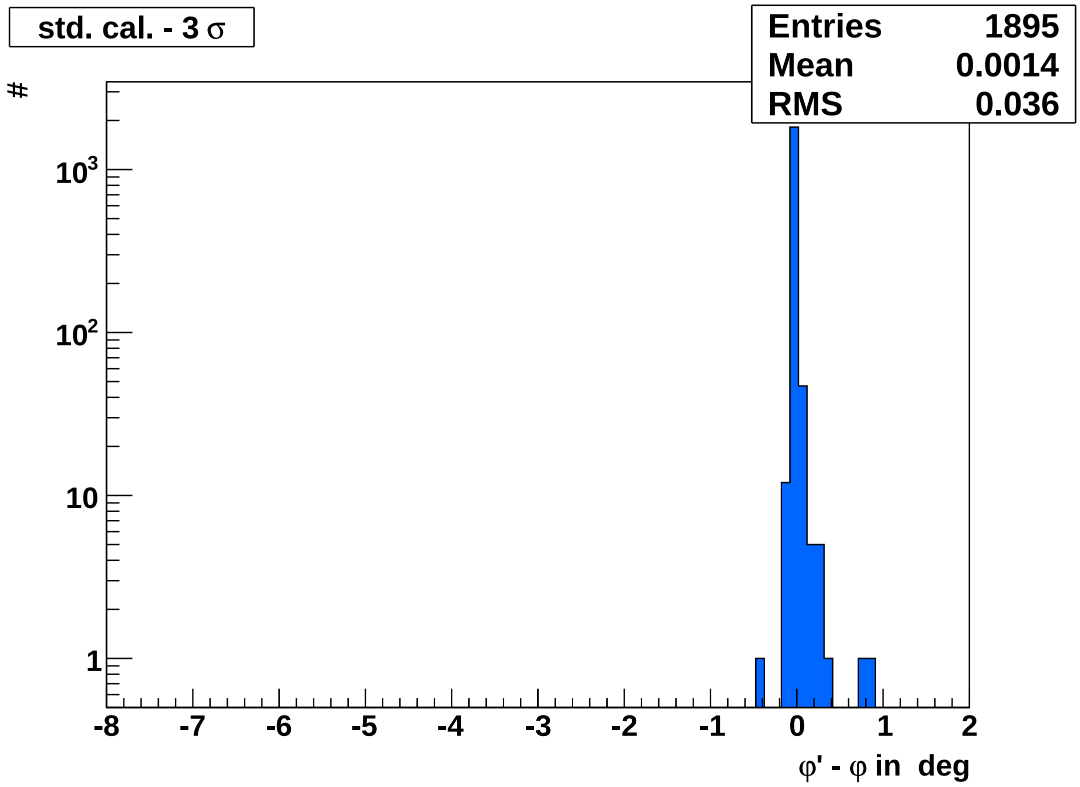

Figure A.2: Histogram of the change of the azimuth angle of the reconstructed shower axis due to the change of the HEAT calibration constants by - 3 standard deviations. φ is the shower azimuth reconstructed with standard calibration whereas φ' is the azimuth reconstructed with changed calibration constants.

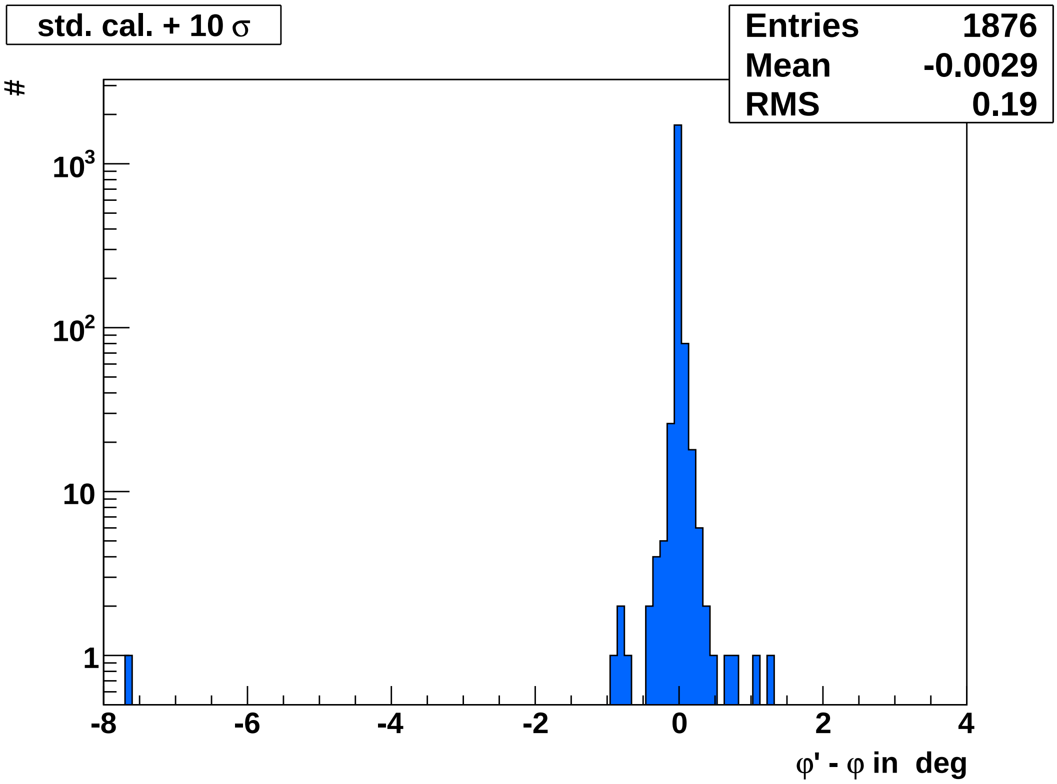

(a) HEAT standard calibration + 10 standard deviations

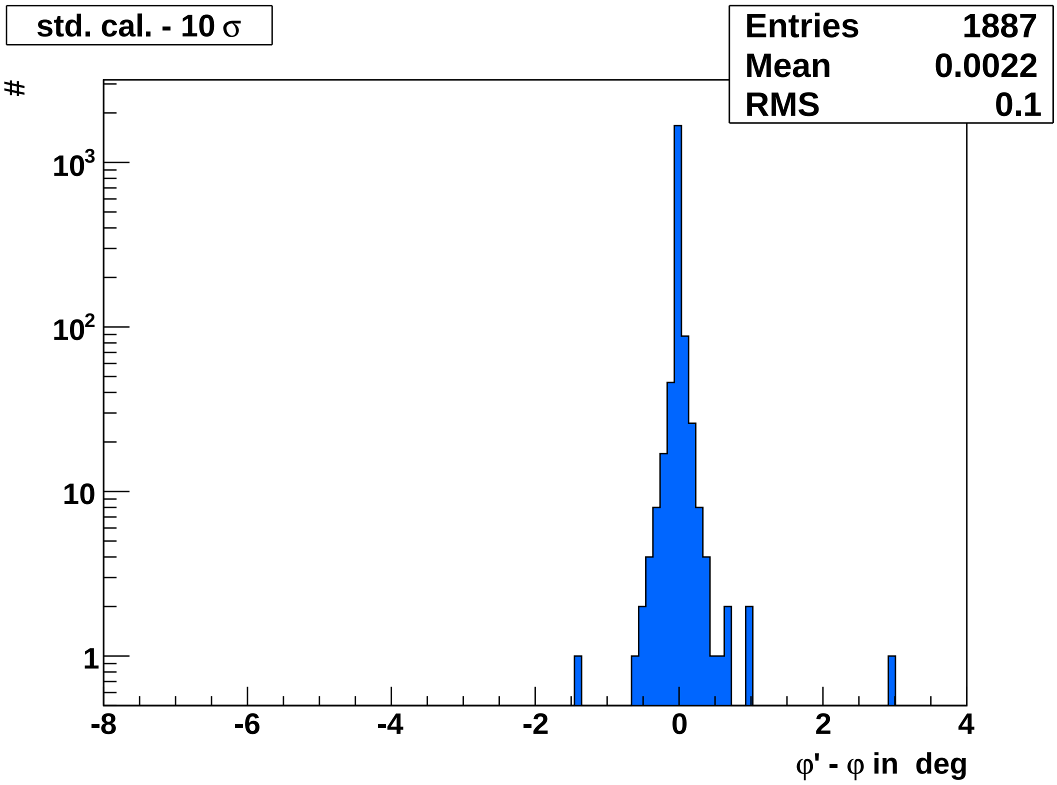

(b) HEAT standard calibration - 10 standard deviations

Figure A.3: Histogram of the change of the azimuth angle of the reconstructed shower axis due to the change of the HEAT calibration constants by ± 10 standard deviations. φ is the shower azimuth reconstructed with standard calibration whereas φ' is the azimuth reconstructed with changed calibration constants.

A.2 Zenith

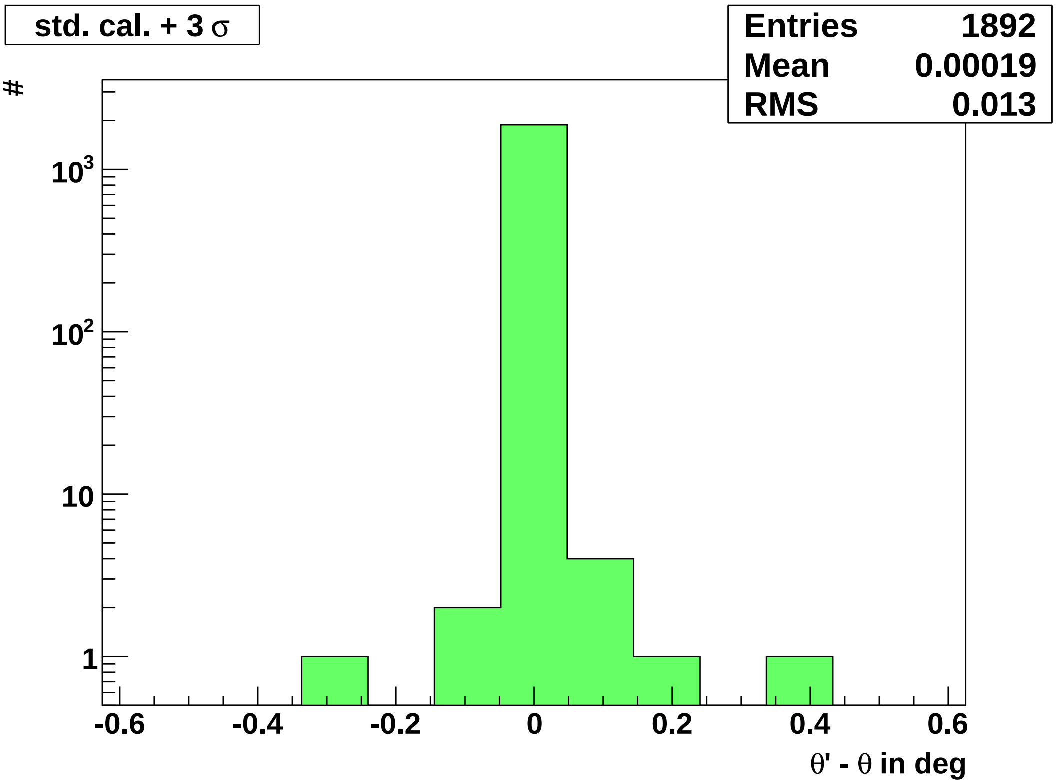

Figure A.4: Histogram of the change of the zenith angle of the reconstructed shower axis due to the change of the HEAT calibration constants by + 3 standard deviations. θ is the shower zenith reconstructed with standard calibration whereas θ' is the zenith reconstructed with changed calibration constants.

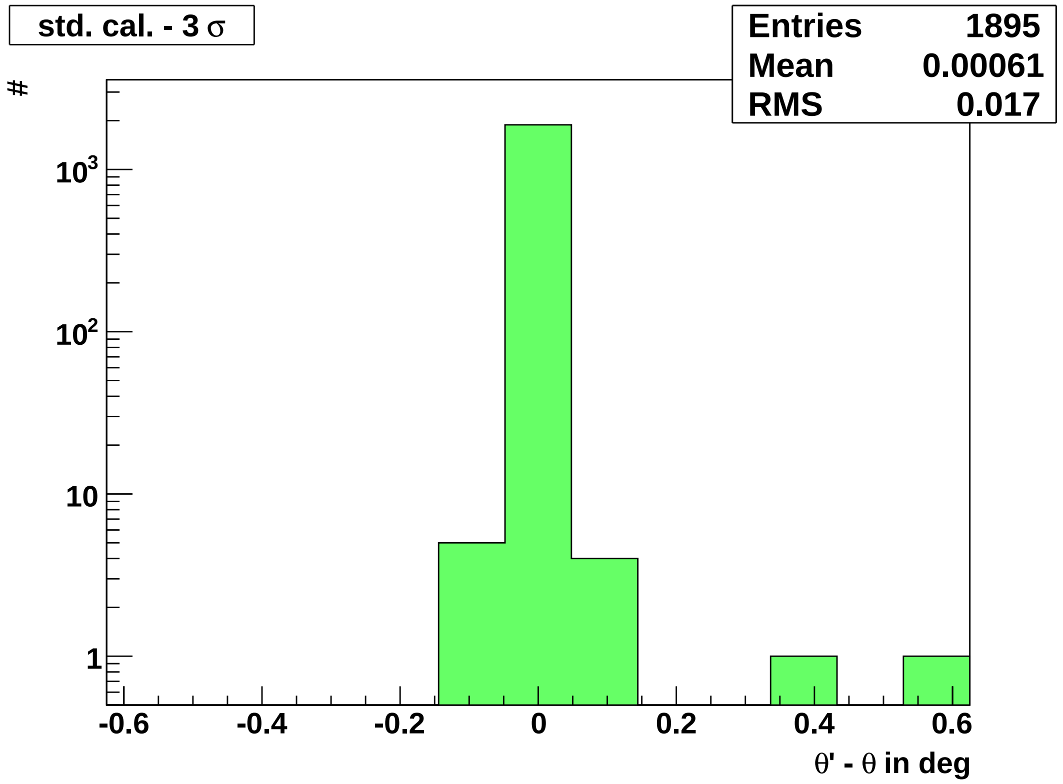

Figure A.5: Histogram of the change of the zenith angle of the reconstructed shower axis due to the change of the HEAT calibration constants by - 3 standard deviations. θ is the shower zenith reconstructed with standard calibration whereas θ' is the zenith reconstructed with changed calibration constants.

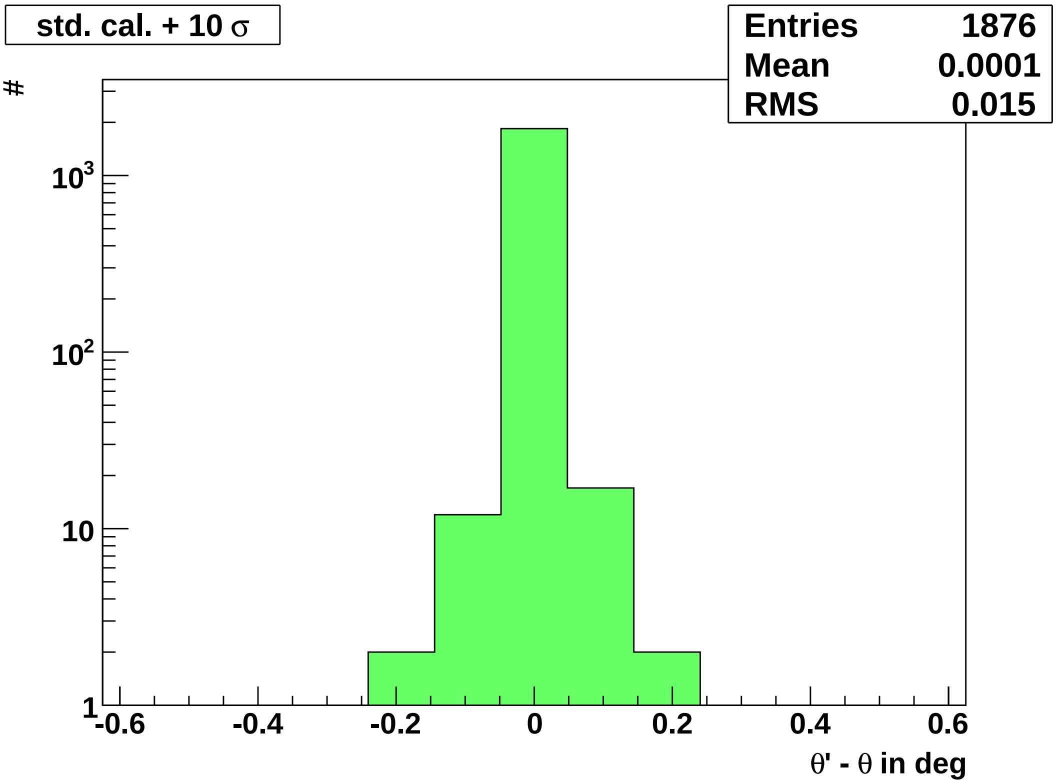

(a) HEAT standard calibration + 10 standard deviations

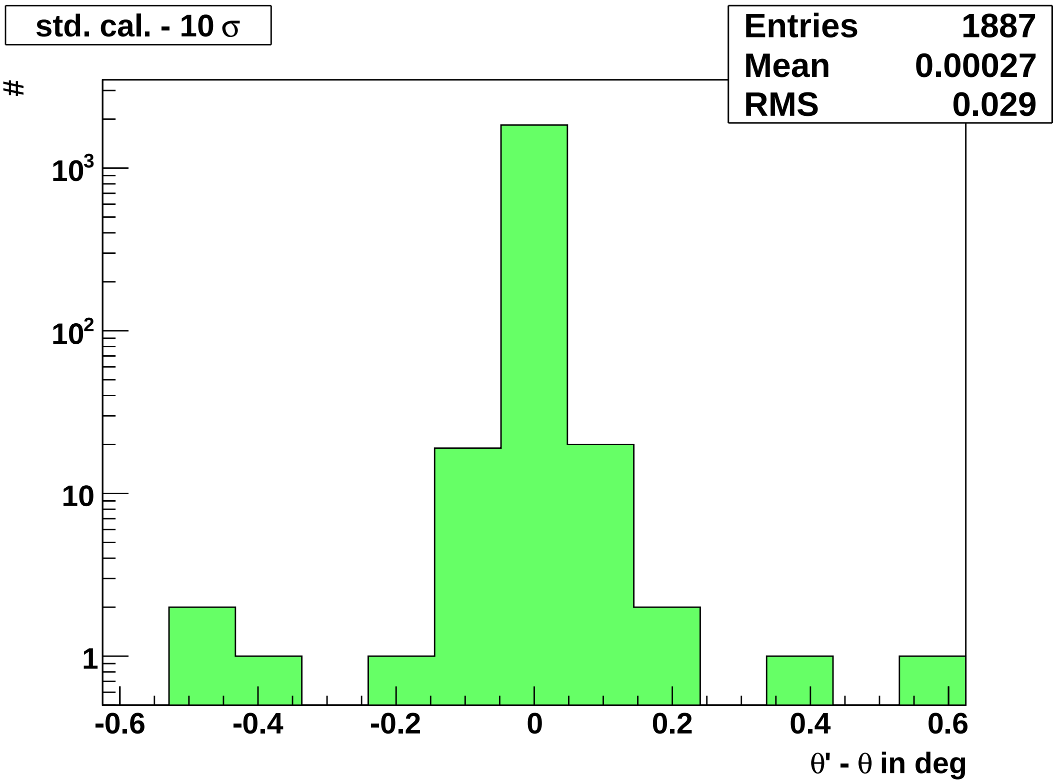

(b) HEAT standard calibration - 10 standard deviations

Figure A.6: Histogram of the change of the zenith angle of the reconstructed shower axis due to the change of the HEAT calibration constants by ± 10 standard deviations. θ is the shower zenith reconstructed with standard calibration whereas θ' is the zenith reconstructed with changed calibration constants.

B. Events per Energy Bin

Δ cal. const.	$\log_{10}(E/\mathrm{eV})$							
σ_{cal}	16.625	16.875	17.125	17.375	17.625	17.875	18.125	18.375
+ 1	3	58	176	160	93	36	8	2
- 1	3	59	180	163	96	38	8	2
+ 3	3	59	180	164	96	38	8	2
- 3	3	59	180	161	96	36	8	2
+ 5	3	60	180	164	95	38	8	2
- 5	3	58	179	161	95	36	8	2
+ 10	3	58	176	159	95	38	8	2
- 10	3	61	181	166	96	38	8	2

Table B.1: Number of HEAT events per energy bin after cuts for each change of the HEAT calibration constants. The energy given is the energy in the middle of the respective energy bin (0.25 decades bin size).

Δ cal. const. / σ_{cal}	$\log_{10}(E/\text{eV})$								
	16.625	16.875	17.125	17.375	17.625	17.875	18.125	18.375	18.625
+ 1	3	55	270	484	536	297	154	52	22
- 1	3	58	273	487	537	297	154	52	22
+ 3	3	59	269	484	537	297	154	53	22
- 3	3	56	273	486	538	297	154	52	22
+ 5	3	56	267	482	536	296	154	53	22
- 5	3	57	272	486	536	297	154	52	22
+ 10	3	56	266	480	533	296	154	53	22
- 10	3	57	270	486	536	297	154	53	22

Table B.2: Number of HEAT and/or Coihueco events per energy bin after cuts for each change of the HEAT calibration constants. The energy given is the energy in the middle of the respective energy bin (0.25 decades bin size).

C. HEAT Participation on CoHe Events

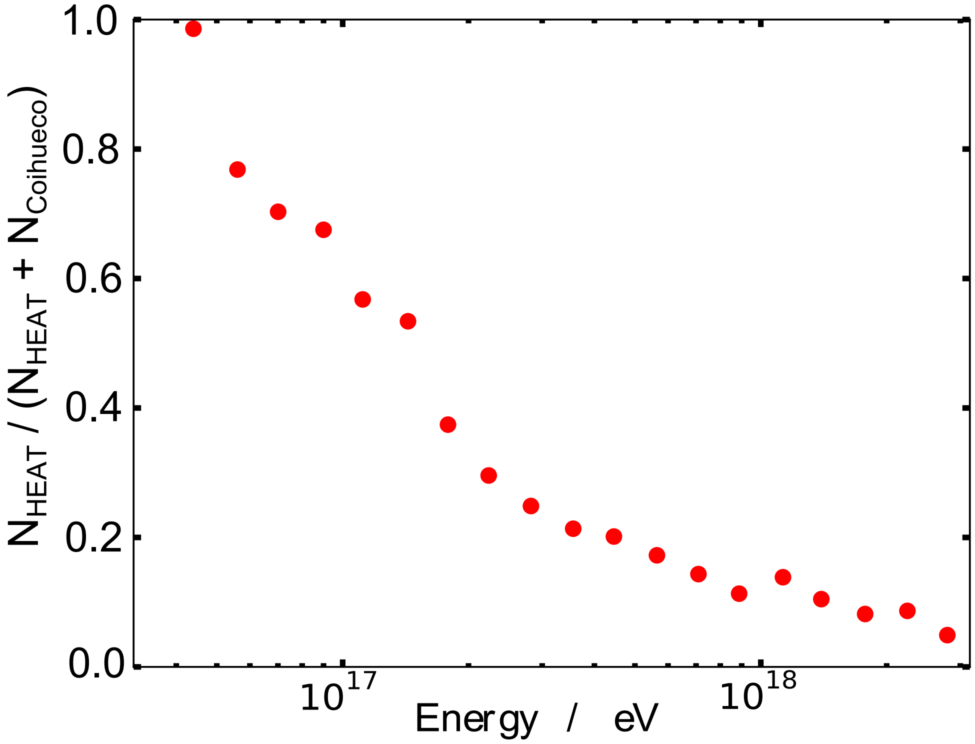

Figure C.1: HEAT participation on CoHe events. N_{HEAT} is the number of triggered HEAT pixels used for the reconstruction of CoHe events in the respective energy bin. N_{Coihueco} is the corresponding number of triggered Coihueco pixels. This plot is based on the data sample taken from 01/12/2010 until 28/02/2011. While low energy showers are mainly seen by HEAT, the fraction of the longitudinal shower profile seen by Coihueco increases for higher energies.

References

[1] V. F. Hess, *Über Beobachtungen der durchdringenden Strahlung bei sieben Freiballonfahrten*, Z. Phys., 13 (1912), p. 1084.

[2] H. L. Bradt and B. Peters, *Investigation of the primary cosmic radiation with nuclear photographic emulsions*, Phys. Rev., 74 (1948), pp. 1828–1837.

[3] P. Auger *et al.*, *Extensive cosmic ray showers*, Rev.Mod.Phys., 11 (1939), pp. 288–291.

[4] A. Bunner, *Cosmic ray detection by atmospheric fluorescence*, PhD thesis, 1967.

[5] J. Blümer, R. Engel, and J. R. Hörandel, *Cosmic rays from the knee to the highest energies*, Progress in Particle and Nuclear Physics, 63 (2009), pp. 293 – 338.

[6] J. R. Hörandel, *Cosmic rays from the knee to the second knee:* 10^{14} *to* 10^{18} *eV*, tech. report, 2007.

[7] R. D. Blandford and J. P. Ostriker, *Particle acceleration by astrophysical shocks*, The Astrophysical Journal Letters, 221 (1978), pp. L29–L32.

[8] V. Berezinsky, M. Kachelriess, and A. Vilenkin, *Ultrahigh-energy cosmic rays without GZK cutoff*, Phys.Rev.Lett., 79 (1997), pp. 4302–4305.

[9] R. Ulrich, R. Engel, and M. Unger, *Hadronic multiparticle production at ultrahigh energies and extensive air showers*, Phys. Rev. D, 83 (2011), p. 054026.

[10] H. J. Bhabha and W. Heitler, *The passage of fast electrons and the theory of cosmic showers*, Proceedings of the Royal Society of London. Series A - Mathematical and Physical Sciences, 159 (1937), pp. 432–458.

[11] J. Matthews, *A Heitler model of extensive air showers*, Astropart.Phys., 22 (2005), pp. 387–397.

[12] Auger Collaboration, *The pierre auger project design report*, (1996).

[13] J. Abraham *et al.*, *Properties and performance of the prototype instrument for the pierre auger observatory*, Nuclear Instruments and Methods in Physics Research Section A: Accelerators, Spectrometers, Detectors and Associated Equipment, 523 (2004), pp. 50 – 95.

[14] J. Abraham *et al.*, Pierre Auger Observatory Collaoration, *Trigger and aperture of the surface detector array of the Pierre Auger Observatory*, Nucl.Instrum.Meth., A613 (2010), pp. 29–39.

[15] J. Abraham *et al.*, *The fluorescence detector of the pierre auger observatory*, Nuclear Instruments and Methods in Physics Research Section A: Accelerators, Spectrometers, Detectors and Associated Equipment, 620 (2010), pp. 227 – 251.

[16] D. Kümpel, *Geometry Reconstruction of Fluorescence Detectors Revisited*, Auger Internal Notes, 99 (2007).

[17] S. Argiro *et al.*, *The Offline framework of the Pierre Auger Observatory*, Nucl. Instr. and Meth., A580 (2007), pp. 1485–1496.

[18] T. Gaisser and A. Hillas, *Reliability of the method of constant intensity cuts for reconstructing the average development of vertical showers*, Proceedings of the 15th International Cosmic Ray Conference, 8 (1977), p. 353.

[19] T. P. et al., *Dependence of the longitudinal shower profile on the characteristics of hadronic multiparticle production*, Proc. 29th Int. Cosmic Ray Conf., 7 (2005), p. 103.

[20] M. Straub, *Mass composition studies with the low energy extension HEAT at the Pierre Auger Observatory*, Auger Internal Notes, (2012).

[21] The Pierre Auger Collaboration, *The Pierre Auger Observatory V: Enhancements*, (2011).

[22] S. Falk *et al.*, *A First Look at HEAT Data*, Auger Internal Notes, 123 (2010).

[23] Offline , *Modules/FdReconstruction/FdSDPFinderOG/FdSDPFinder.cc*, SVN-Trunk rev. 18737.

[24] Offline , *ADST/RecEvent/src/FdRecPixel.h*, SVN-Trunk rev. 21010M.

[25] F. Arqueros, J. Hörandel, and B. Keilhauer, *Air fluorescence relevant for cosmic-ray detection, Summary of the 5th fluorescence workshop, El Escorial 2007*, Nuclear Instruments and Methods in Physics Research Section A: Accelerators, Spectrometers, Detectors and Associated Equipment, 597 (2008), pp. 1 – 22. Proceedings of the 5th Fluorescence Workshop.

Erklärung

Hiermit versichere ich, dass ich diese Arbeit einschließlich beigefügter Zeichnungen, Darstellungen und Tabellen selbstständig angefertigt und keine anderen als die angegebenen Hilfsmittel und Quellen verwendet habe. Alle Stellen, die dem Wortlaut oder dem Sinn nach anderen Werken entnommen sind, habe ich in jedem einzelnen Fall unter genauer Angabe der Quelle deutlich als Entlehnung kenntlich gemacht.

Aachen, den 27. August 2012

Oskar Hofmann